Spatiotemporal variations of surface deformation, shallow creep rate, and slip partitioning between the San Andreas and southern Calaveras Fault

Yuexin Li[1], Roland Burgmann[1], and Taka'aki Taira[1]

[1]University of California, Berkeley

November 22, 2022

Abstract

The Calaveras Fault (CF) branches from the San Andreas Fault (SAF) near San Benito, extending sub-parallel to the SAF for about 50 km with only 2-6 km separation and diverging northeastward. Both the SAF and CF are partially coupled, exhibit spatially variable aseismic creep and have hosted moderate to large earthquakes in recent decades. Understanding how slip partitions among the main fault strands of the SAF system and establishing their degree of coupling is crucial for seismic hazard evaluation. We perform a timeseries analysis using more than 5 years of Sentinel-1 data covering the Bay Area (May 2015-October 2020), specifically targeting the spatiotemporal variations of creep rates around the SAF-CF junction. We derive the surface creep rates from cross-fault InSAR timeseries differences along the SAF and CF including adjacent Sargent and Quien Sabe Faults. We show that the variable creep rates (0-20 mm/yr) at the SAF-CF junction are to first order controlled by the angle between the fault strike and the background stress orientation. We further examine the spatiotemporal variation of creep rates along the SAF and CF and find a multi-annual coupling increase during 2016-2018 the subparallel sections of both faults, with the CF coupling change lagging behind the SAF by 3 to 6 months. Similar temporal variations are also observed in both b-values inferred from declustered seismicity and aseismic slip rates inferred from characteristic repeating earthquakes. The high correlation of b-value and slip-rate changes may indicate that the SAF is extremely sensitive to small stress perturbations.

Hosted file

`essoar.10512336.1.docx` available at https://authorea.com/users/540230/articles/600165-spatiotemporal-variations-of-surface-deformation-shallow-creep-rate-and-slip-partitioning-between-the-san-andreas-and-southern-calaveras-fault

Posted on 22 Nov 2022 — CC-BY-NC 4 — https://doi.org/10.1002/essoar.10512336.1 — This a preprint and has not been peer reviewed. Data may be preliminary.

Spatiotemporal variations of surface deformation, shallow creep rate, and slip partitioning between the San Andreas and southern Calaveras Fault

Yuexin Li[1], Roland Bürgmann[1] and Taka'aki Taira[1]

[1] Department of Earth and Planetary Science and Berkeley Seismology Laboratory, University of California, Berkeley, CA, USA.

Corresponding author: Yuexin Li (yuexinli@berkeley.edu)

Key Points:

- Obtained velocity and deformation timeseries along the SAF-CF junction using Sentinel-1 interferograms from 2015 to 2020
- Delineated detailed spatial distribution of creep rates on major Bay Area Faults
- InSAR timeseries capture fault coupling increases along the SAF and CF, correlated with repeating earthquakes and b-values variations

Abstract

The Calaveras Fault (CF) branches from the San Andreas Fault (SAF) near San Benito, extending sub-parallel to the SAF for about 50 km with only 2-6 km separation and diverging northeastward. Both the SAF and CF are partially coupled, exhibit spatially variable aseismic creep and have hosted moderate to large earthquakes in recent decades. Understanding how slip partitions among the main fault strands of the SAF system and establishing their degree of coupling is crucial for seismic hazard evaluation. We perform a timeseries analysis using more than 5 years of Sentinel-1 data covering the Bay Area (May 2015-October 2020), specifically targeting the spatiotemporal variations of creep rates around the SAF-CF junction. We derive the surface creep rates from cross-fault InSAR timeseries differences along the SAF and CF including adjacent Sargent and Quien Sabe Faults. We show that the variable creep rates (0-20 mm/yr) at the SAF-CF junction are to first order controlled by the angle between the fault strike and the background stress orientation. We further examine the spatiotemporal variation of creep rates along the SAF and CF and find a multi-annual coupling increase during 2016-2018 the subparallel sections of both faults, with the CF coupling change lagging behind the SAF by 3 to 6 months. Similar temporal variations are also observed in both b-values inferred from declustered seismicity and aseismic slip rates inferred from characteristic repeating earthquakes. The high correlation of b-value and slip-rate changes may indicate that the SAF is extremely sensitive to small stress perturbations.

Plain Language Summary

The San Andreas Fault (SAF) takes up most plate motion between the Pacific and North American plates. The southern Calaveras Fault (CF) branches from

the SAF near San Benito, being subparallel to the main SAF with only 2-6 km separation for about 50 km. Both faults are slipping aseismically at the surface with variable rates. It is unusual to observe two rapidly creeping faults that are so close to each other. We delineate fault creep rates, that is, how fast the faults are slipping at the surface on major Bay Area faults considering more than 5 years of remote sensing images timeseries. We find that the fault creep rate is to first order controlled by fault geometry and regional tectonics. In addition, we observe a slowdown in fault creep during 2016-2018 on the SAF, confirmed by analysis of clusters of small earthquakes and repeating earthquakes that have nearly identical seismic waveforms. This may indicate that the SAF is extremely sensitive to small loading perturbations. Our study shows remote sensing techniques are capable of monitoring subtle large-scale ground deformation with good spatial and temporal accuracy, which is crucial for monitoring fault slip behaviors and assessing seismic hazard.

1 Introduction

The 1100-km-long San Andreas Fault (SAF) system extends from the Gulf of California in the southeast to the Mendocino triple junction in the northwest (Wallace, 1990). Between San Juan Bautista and Parkfield lies the 150-km-long central creeping section, where the majority of the 38 mm/yr right-lateral plate motion between the Sierra-Nevada Great-Valley block and Pacific plate (d'Alessio et al., 2005) is accommodated through aseismic slip (Savage & Burford, 1973; Ryder & Bürgmann, 2008; Jolivet et al., 2015; Khoshmanesh et al., 2015). The Calaveras Fault (CF) branches from the SAF at the northern transition zone, extends sub-parallel to the SAF for about 50 km, with only 2-6 km separation from Paicines to San Benito (Figure 1), and diverges away from the SAF further north (Watt et al., 2014). At the SAF-CF junction where the two faults are sub-parallel, the distribution of microseismicity indicates that the SAF is nearly vertical, the CF is dipping to the southwest, and the two faults are possibly connected at depth (Watt et al., 2014). The two faults take up the majority of the plate motion, and both faults exhibit shallow creep (e.g. Burford & Harsh, 1980; Galehouse & Lienkaemper, 2003; Johanson & Bürgmann, 2005; Tong et al., 2013; Scott et al., 2020). Additionally, a modest part of the slip budget is partitioned onto the Sargent Fault (SF) and Quien Sabe Fault (QSF) (Prescott & Burford, 1976; Templeton et al., 2008; Mongovin & Philibosian, 2021).

Both the SAF and CF are partially coupled at the SAF-CF junction and have hosted moderate to large earthquakes in the past decades (Johanson & Bürgmann, 2005; Oppenheimer et al., 1990). Creep rates on the SAF taper off to zero at the northern transition zone, and the fault remains fully locked to the north, where it hosted the 1989 M6.9 Loma Prieta and 1906 M7.9 San Francisco earthquakes (Thatcher et al., 1997; Zhang et al., 2018). Being one of the most seismically active branches of the SAF system, the CF hosted a sequence of four northward progressing earthquakes, including the 1979 M5.9 Coyote Lake earthquake, the 1984 M6.2 Morgan Hill earthquake, the 1988 M5.1 Alum Rock

earthquake, and the 2007 M5.6 Alum Rock earthquake (Oppenheimer et al., 1990; Du & Aydin, 1993; Toppozada et al., 2002; Murray-Moraleda & Simpson, 2009).

Spatiotemporally variable creep on the SAF and CF has been documented by alignment array (Burford & Harsh, 1980; Lisowski & Prescott, 1981; Lienkaemper & Prescott, 1989) and creepmeter measurements (Schulz, 1989; Bokelmann & Kovach, 2003; Bilham et al., 2004) since the 1960s. While alignment-array and creepmeter measurements provide decades of accurate records of shallow fault creep, the spatial extent of creep mapping is largely limited by the sparsely distributed locations of these geodetic sites. A detailed assessment of the spatiotemporal distribution of fault creep along the SAF system, especially at the transition zone, is crucial for seismic hazard evaluation in the densely populated San Francisco Bay Area (e.g. Field et al., 2014; Harris, 2017).

Interferometric Synthetic Aperture Radar (InSAR) is a powerful geodetic tool capable of measuring large-scale ground deformation at high spatial resolution (<100 m) with sub-centimeter accuracy. In recent decades, interseismic deformation at the SAF-CF junction has been measured through the ERS (1992-2001, e.g. Johanson & Bürgmann, 2005; Ryder & Bürgmann, 2008) and Envisat (2003-2010, e.g. Turner et al., 2015) satellites launched by the European Space Agency (ESA), as well as the ALOS mission (2006-2010, e.g. Tong et al., 2013; Jolivet et al., 2015) launched by the Japan Aerospace Exploration Agency. The minimum image acquisition intervals of these systems ranged from 35-46 days, but there were often longer gaps in data collection. Due to the limited number of radar acquisitions, only rate information of fault slip around the SAF-CF junction had been previously extracted through stacking (e.g. Ryder & Bürgmann, 2008) and timeseries analysis (e.g. Jolivet et al., 2015). With the launch of the Sentinel-1A, B constellation in 2014 and 2016 by ESA, the recurrence interval in the study region is reduced to 12 days, making it possible to delineate both spatial and temporal behaviors of fault creep.

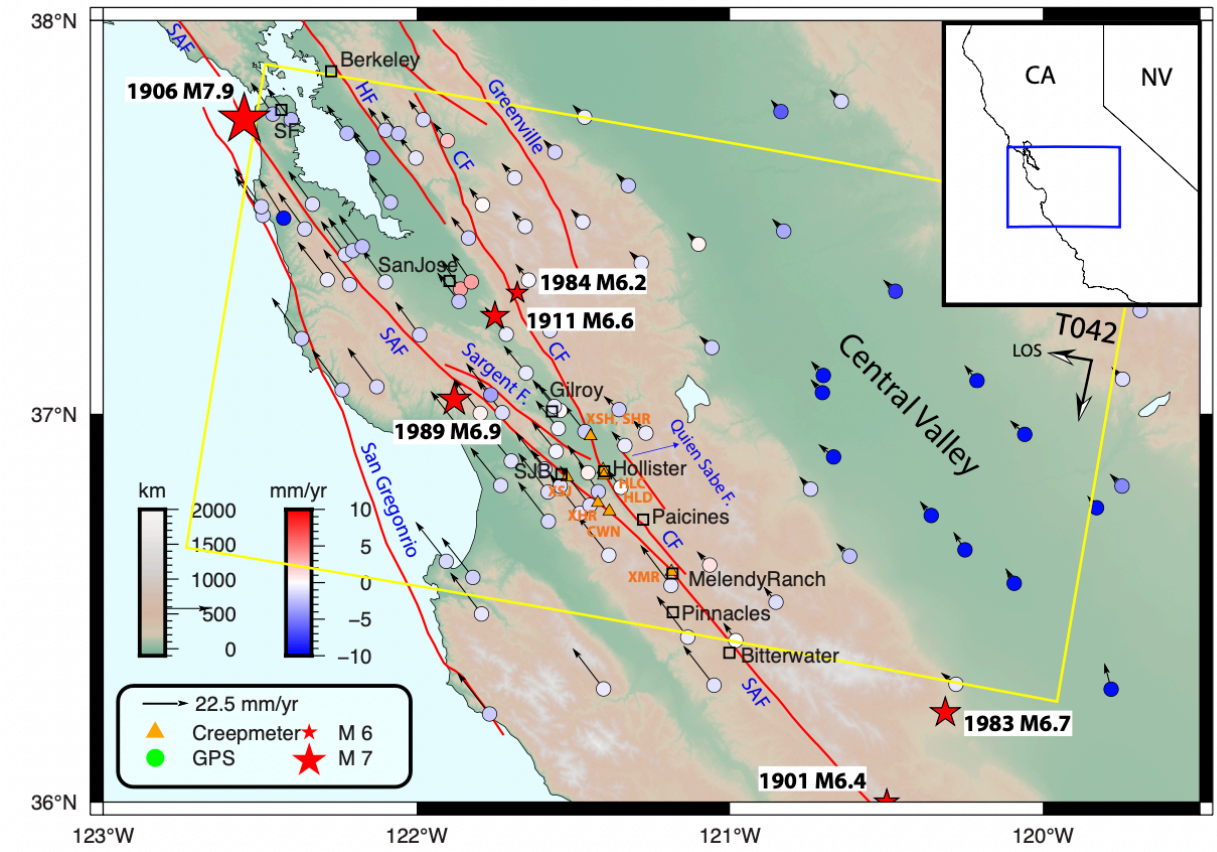

Figure 1 Overview map of the study region. The yellow rectangle shows the spatial footprint of the Sentinel-1 InSAR coverage. Black arrows show the horizontal velocity field in the North American reference frame, derived from GPS timeseries spanning the InSAR observation period from the Nevada Geodetic Laboratory (Kreemer et al., 2014; Blewitt et al., 2018). Vertical rates at GPS sites are shown by colored circles. Note that the color for stations in the Central Valley is saturated due to rapid subsidence in excess of 10 mm/yr. Major faults are shown in red lines. SAF: San Andreas Fault, CF: Calaveras Fault, HF: Hayward Fault. Epicenters of historical M>6 earthquakes since 1900 from USGS are shown as red stars. Locations of creepmeters on the SAF and CF at the SAF-CF junction are shown as orange triangles.

Various factors have been proposed to control fault creep (Harris, 2017; Bürgmann, 2018) Serpentinite has been found along several California creeping faults (Harris, 2017), and laboratory experiments show that the mineral talc in serpentine significantly reduces the fault strength due to its special frictional properties (Moore & Rymer, 2007). Other creeping faults contain mixtures of clays and other velocity-strengthening and low-friction minerals, and high fluid

pressure, or low effective normal stress, is also understood to favor aseismic fault slip (Bürgmann, 2018 and references cited therein).

Nearby earthquakes can accelerate or suppress creep on Bay Area faults due to static stress changes (Lienkaemper et al., 1997; Bokelmann & Kovach, 2003). In terms of the temporal variability of fault creep, episodic slip rate changes on the Central SAF have been proposed to be driven by pore pressure variations (Khoshmanesh & Shirzaei, 2018) and modulated by rainfall as well as other seasonal effects (Roeloffs, 2001). Shallow aseismic slip transients can be dynamically triggered by remote earthquakes (Tymofyeyeva et al., 2019), and the presence of shallow accelerated creep can be a lingering effect of decaying postseismic deformation from nearby large earthquakes (Bokelmann & Kovach, 2003).

In addition to geodetic datasets, seismological observations can also provide a unique perspective of fault creep at depth. Spatiotemporal variability of aseismic fault creep can be inferred from characteristic repeating earthquakes (CREs, Nadeau & Johnson, 1998; Nadeau & McEvilly, 2004; Uchida & Bürgmann, 2019). Moreover, a recent study by Liu et al. (2022) shows that the distribution of fault creep rates can be directly linked to spatial variations in the fraction of non-clustered seismicity and in b-values.

In this study, we aim to update the interseismic velocity map over the southern San Francisco Bay Area using more than 5 years of Sentinel-1 data through systematic InSAR timeseries analysis. We benchmark our InSAR results with multiple complementary datasets, including alignment arrays, creepmeters, and Global Positioning System (GPS) timeseries. We assess the spatiotemporal behavior of the tectonic and non-tectonic deformation and discuss the slip partitioning between major faults in the SAF-CF junction. Then, we obtain up-to-date creep rate estimates along the SAF and CF at the CF-SAF junction and obtain a detailed mapping of creep behaviors in space and time through the transition zone. We evaluate temporal variations of creep rates on annual and multi-annual time scales. The multi-annual changes of surface creep rates are further compared with temporal changes of seismicity, CREs, and b-values.

2 Data and Methods

2.1 InSAR Data and Processing

We use all available Sentinel-1 SAR data collected from descending track 42 covering the study region. The spatial footprint of the SAR coverage is shown in Figure 1. A total of 133 images were acquired between May 2015 and October 2020. The InSAR data are processed using the GMTSAR software (Sandwell et al., 2011a, 2011b). We use both short-term and 1-year interferograms to form the interferogram network (Figure S1). For each SAR acquisition, we form interferograms with its five nearest scenes before and after the acquisition; that is, a total of 10 links for each acquisition. No perpendicular-baseline restriction is set when forming the short-term interferograms. To limit the potential phase bias in short-term interferograms (fading signal, Ansari et al., 2021), we add

1-year pairs (350-380 days temporal baseline) with <50 m perpendicular orbit baseline to the network. This leads to a total of 739 interferograms for short- (650) and long-term (89) temporal baselines.

All interferograms are geometrically aligned with reference acquisition 20180426. We remove topographic phase contributions using the 30 m SRTM-1 digital elevation model (Farr et al., 2007). We decimate the interferograms 16 and 4 times in range and azimuth direction, respectively, leading to a ~60x80 m pixel resolution. A 200 m Gaussian filter and adaptive Goldstein filter (Goldstein & Werner, 1998) are applied on the interferograms. The interferograms are unwrapped using the Statistical-cost, Network-flow Algorithm for Phase Unwrapping software (SNAPHU, Chen & Zebker, 2002) with an average coherence mask of 0.2 (Figure S2). Then, all interferograms are geocoded with a pixel spacing of 60 m.

Tropospheric delay is a major error source for C-band interferometry, and its contribution can be estimated and mitigated through auxiliary information from weather models (e.g. Berrada Baby et al., 1988; Jolivet et al., 2011; Bekaert et al., 2015). The new generation of the ERA5 weather model (Hersbach et al., 2020) delivered by the European Center for Medium-Range Weather Forecasts (ECMWF) provides hourly solutions of temperature and relatively humidity in 137 vertical pressure levels with 31-km spatial resolution. Here we follow the method described in Jolivet et al. (2011) to correct for the atmospheric delay in each interferogram using the ERA5 weather model products. The ERA5 correction effectively reduces 37% of the variance in the interferograms after ramp removal (Figure S3). All interferograms are referenced to a 10-by-10 pixel area near GPS station LUTZ, located on a central bedrock exposure in the southern Santa Clara Valley (Figure 1). We perform timeseries analysis on interferograms after ERA5 correction using the Small BAseline Subset method (SBAS; Berardino et al., 2002; Schmidt & Bürgmann, 2003). The timeseries product is further cleaned using the Common Scene Stacking method (CSS, Tymofyeyeva & Fialko, 2015) for the removal of remaining, temporally uncorrelated atmospheric noise. Finally, we estimate the average velocity and corresponding uncertainties from the timeseries using linear least squares regression. Note that the CSS method may smooth out the seasonal cycles on the InSAR timeseries (e.g., Figure S9, station P242), therefore, to better quantify and preserve the temporal behaviors along the faults, we use timeseries results before applying the CSS method in Section 3.1 and Section 3.3.

2.2 GPS Timeseries and Processing

We download GPS daily solution timeseries from the Nevada Geodetic Laboratory (Blewitt et al., 2018) in the North American plate reference frame (Kreemer et al., 2014). A total of 75 stations that collected continuous data during the InSAR observation period (May 2015 – October 2020) within the InSAR footprint are selected. For the comparison with InSAR, we reference the 3-component displacement timeseries of all stations to GPS station LUTZ. Next, we estimate their secular velocities and corresponding uncertainty in the east, north, and vertical direction, respectively. Then, the 3-component velocities and timeseries

are projected into the InSAR line of sight (LOS) direction, based on the local look vector at each GPS station. Note that we keep the GPS timeseries in the North American reference frame when modeling seasonal loading parameters in Section 3.1.

2.3 Creepmeter timeseries and alignment array data

To validate the InSAR average rate and temporal behavior of fault creep, we download creepmeter timeseries from USGS (https://earthquake.usgs.gov/monitoring/deformation/data/download.php). For the SAF, daily solution timeseries from three stations (XSJ2, XHR2, CWC3) and 10-minute solution timeseries from 4 stations (XSJ3, XHR3, CWN1, XMR1) are available for 1985-2020. On the other hand, for the four stations on the CF (XSH1, SHR1, HLC1, HLD1), only manual measurements that were surveyed several times a year are available for the period spanning 1985-2015. Long-term creepmeter timeseries on the SAF and CF used in this study are shown in Figure S4. Creep rates on the SAF increased immediately after the 1989 Loma Prieta earthquake, whereas fault creep on the CF was suppressed for ~10 years following the event. Considering the time-dependent nature of the creepmeter records, we divide the creepmeter data into four time periods (1985-1989, 1989-2000, 2000-2015, 2015-2020) and estimate the rates separately (Table S4). Note that creepmeter measurements are not available on the CF for the InSAR period (2015-2020). Therefore, we only compare creepmeter timeseries on the SAF with our InSAR timeseries in Figure 3.

In addition to creepmeter timeseries, we collected published creep rates from alignment array measurements at the SAF-CF junction (e.g. Burford & Harsh, 1980; Lisowski & Prescott, 1981; Galehouse & Lienkaemper, 2003; Titus et al., 2006**;** McFarland et al, 2017). A complete summary and references of the data sources can be found in Table S4.

2.4 Seismicity, catalog declustering and b-value estimation

We download the double-difference seismic catalog from the Northern California Earthquake Data Center (NCEDC) from 1984 to 2021 (Waldhauser & Schaff, 2008; Waldhauser, 2009). To investigate the spatiotemporal variation of the background seismicity rate, we use the nearest-neighbor approach (Zaliapin & Ben-Zion, 2013; Johnson et al., 2017) to decluster the seismic catalog and exclude the effect of dependent aftershocks on the b-value estimation. We calculate the nearest distance η_{ij} between event pairs (Eq 1) from the rescaled time T_{ij} and distance R_{ij} to identify clustered events in the catalog.

$$\eta_{ij} = T_{ij} R_{ij} \text{ (Eq 1)}$$

$$T_{ij} = t_{ij} 10^{-qbm_i} \text{ (Eq 2)}$$

$$R_{ij} = \left(r_{ij}\right)^{d_f} 10^{-(1-q)bm_i} \text{ (Eq 3)}$$

For each event pair, the rescaled time T_{ij} is a function of interevent time t_{ij}, b-value b, event magnitude m_i, and scaling factor q (Eq 2). The rescaled distance

is a function of event distance r_{ij}, b-value b, event magnitude m_i, scaling factor q and distance scaling factor d_f (Eq 3). Here, we use $b = 1$, $q = 0.5$, $d_f = 1.6$ for the nearest-neighbor distance calculation (Johnson et al., 2017).

We calculate the nearest distance η_{ij} for event pairs of all magnitudes. The distribution of nearest-neighbor distances, and the nearest-neighbor rescaled time and distance plot are shown in Figure S5. We observe a bimodal distribution of the clustered and background seismicity. The clustered events are close in space and time, therefore have smaller nearest-neighbor distances than the background seismicity. We eliminate the clustered seismicity by removing all events with $\eta < 1.25 \times 10^{-6}$. The comparison between the original (96148 events) and declustered (51324 events) catalogs is shown in Figure S6.

We estimate b-values using the original and declustered catalogs. The frequency-magnitude distribution of the seismicity can be described by the Gutenberg-Richter law (Eq 4, Gutenberg & Richter, 1944), where N is the cumulative number of events larger than a given magnitude M. The constants a and b are the a-value and b-value, where the a-value is a representation of the overall seismicity level, and the b-value is the slope of the distribution, reflecting the relative number of larger- and smaller-magnitude events. The magnitude of completeness M_c is estimated using the maximum curvature method (MAXC) (Wiemer & Wyss, 2000), where we define M_c as the magnitude that has the maximum non-cumulative number of events.

$$\log_{10} N = a - bM, \quad M \geq M_c \text{ (Eq 4)}$$

2.5 Aseismic fault slip inferred from characteristic repeating earthquakes

We use the Northern California Seismic System (NCSS) waveform catalog to search for CREs. The CREs have nearly identical seismic waveforms and locations, and are believed to repeatedly rupture the same asperity on a fault (Uchida & Bürgmann, 2019). Following our previous studies (Shirzaei et al., 2013; Taira et al., 2014), a waveform coherency analysis was performed to identify CREs. As M_c in our target region is around 1.0 (Tormann et al., 2014), we used earthquakes with M 1.0 from the NCSS catalog during 1984-2019. A total of 70,335 earthquakes were analyzed. For each earthquake, we download seismic records from stations that are located within 35-km from the epicenter. Our analysis used vertical-component data from either broadband sensors or short-period geophones. The waveform coherence was measured with a 10.24-sec data window from the direct P-wave in the frequency band 8-24 Hz. This 10.24-sec window includes S waves and coda waves, and the frequency band was selected to suppress false detections of CREs with M ~1.0 following (Uchida, 2019). As the horizontal location errors for the majority of earthquakes in our target area is less than 3 km, our coherency analysis was applied only for pairs of earthquakes where catalog event separations (horizontally) are less than 3 km. Following previous work (e.g., Materna et al., 2018), CREs were identified if two or more stations meet a coherency threshold to ensure waveform similarity. We used four different coherency thresholds: 0.95, 0.96, 0.965, and 0.97. In this

manuscript, we used the CRE detections with our highest threshold (0.97) to minimize false detection. A total of 19793 CREs in 3547 sequences are detected during 1984-2019.

For each CRE sequence, we can infer the slip from the event magnitude using the empirical relation proposed by Nadeau & Johnson (1998) (Eq 5), where d is the slip in the event and inferred aseismic slip driving the CRE recurrence, and M_0 is the seismic moment of the CREs. The seismic moment M_0 is calibrated from the moment-magnitude relationship (Eq 6, Hanks & Kanamori, 1979). We estimated the slip on a given fault section by averaging the slip among all sequences within the section, and reconstructed the cumulative slip history from CREs following the procedures described in Nadeau & McEvilly (2004).

$$\log_{10}(d) = -2.36 + 0.17 \log_{10}(M_0) \quad \text{(Eq 5)}$$

$$\log(\mathbf{M_0}) = \mathbf{16.1} + \mathbf{1.5M_w} \text{ (Eq 6)}$$

3 Results

3.1 Average InSAR LOS velocity, timeseries, and validations

The InSAR LOS velocity map derived from the timeseries analysis is shown in Figure 2a, and its corresponding uncertainty map is shown in Figure S7. Our Sentinel-1 velocity map reveals similar ground deformation features as have been identified in previous InSAR studies, including the tectonic fault motion of the San Andreas Fault system (e.g. Johanson & Bürgmann, 2005; Ryder & Bürgmann, 2008; Tong et al., 2013), elastic aquifer deformation due to groundwater-level changes in the Santa Clara Valley (e.g. Schmidt & Bürgmann, 2003; Chaussard et al., 2014; Chaussard et al., 2017), and rapid subsidence in the Central Valley due to unsustainable agricultural pumping (e.g. Ojha et al., 2018; Liu et al., 2019). The InSAR LOS velocities agree well with the projected 3D GPS velocities (Figure 2a) with a 1.39 mm/yr standard deviation of the LOS rate differences (Figure 2b, c). A complimentary comparison between InSAR and 2D (horizontal only) GPS LOS velocities leads to a 1.46 mm/yr standard deviation of the velocity differences (Figure S8). Note that nine stations are excluded from the analysis, including seven stations experiencing severe subsidence within the Central Valley and two stations in coastal areas that have extremely poor InSAR coherence (Table S2).

The InSAR timeseries are further validated with creepmeter and GPS timeseries. For comparison with creepmeter measurements, we use InSAR timeseries averaged from 0.5-by-1.5km boxes on each side of the fault and compare the cross-fault InSAR-timeseries differences with the creepmeter data, assuming fault-parallel strike-slip offsets (Figure 3a, b). The cross-fault InSAR timeseries agree with the creepmeter data with standard deviations of 6.92 mm, 9.71 mm, 8.01 mm and 20.89 mm for station XMR1, CWN1, XHR3, XSJ3, respectively. For comparison with the GPS timeseries, we average the InSAR timeseries from 10-by-10 pixel areas that are collocated with the GPS sites. In the comparison, both InSAR and GPS are referenced to GPS station LUTZ. Examples of InSAR

and GPS timeseries collocated at GPS sites around the SAF-CF junction (Figure 3a) are shown in Figure 3c. Comparisons of InSAR and GPS timeseries at all GPS sites are shown in Figure S9. The InSAR timeseries agrees with GPS timeseries with average standard deviation of 4.1 mm (with CSS) and 13.5 mm (without CSS), respectively.

As mentioned above, the InSAR timeseries include contributions from multiple sources, including tectonic fault motion and non-tectonic hydrological deformation processes (including elastic surface loading and poroelastic aquifer deformation) that often have a seasonal pattern. To better evaluate the temporal behaviors of non-tectonic deformation and its effect on the assessment of fault behavior, we model the InSAR and GPS displacement timeseries using Eq 7, after realizing a North American reference frame (Amos et al., 2014; Materna et al., 2021), where A-F are coefficients of the loading terms, and is the angular frequency of the annual seasonal loading. We put our InSAR timeseries into a North American reference frame by finding the best-fitting model parameters (Eq 7) for the reference GPS station LUTZ and adding the modeled seasonal cycle to all InSAR timeseries. This assists in the visualization of regional hydrological loading signals in seasonal amplitude and phase maps (e.g., Amos et al., 2014). Then, the amplitude and timing (phase) of the maximum seasonal uplift can be estimated from Eq 8, 9 (Figure 4a).

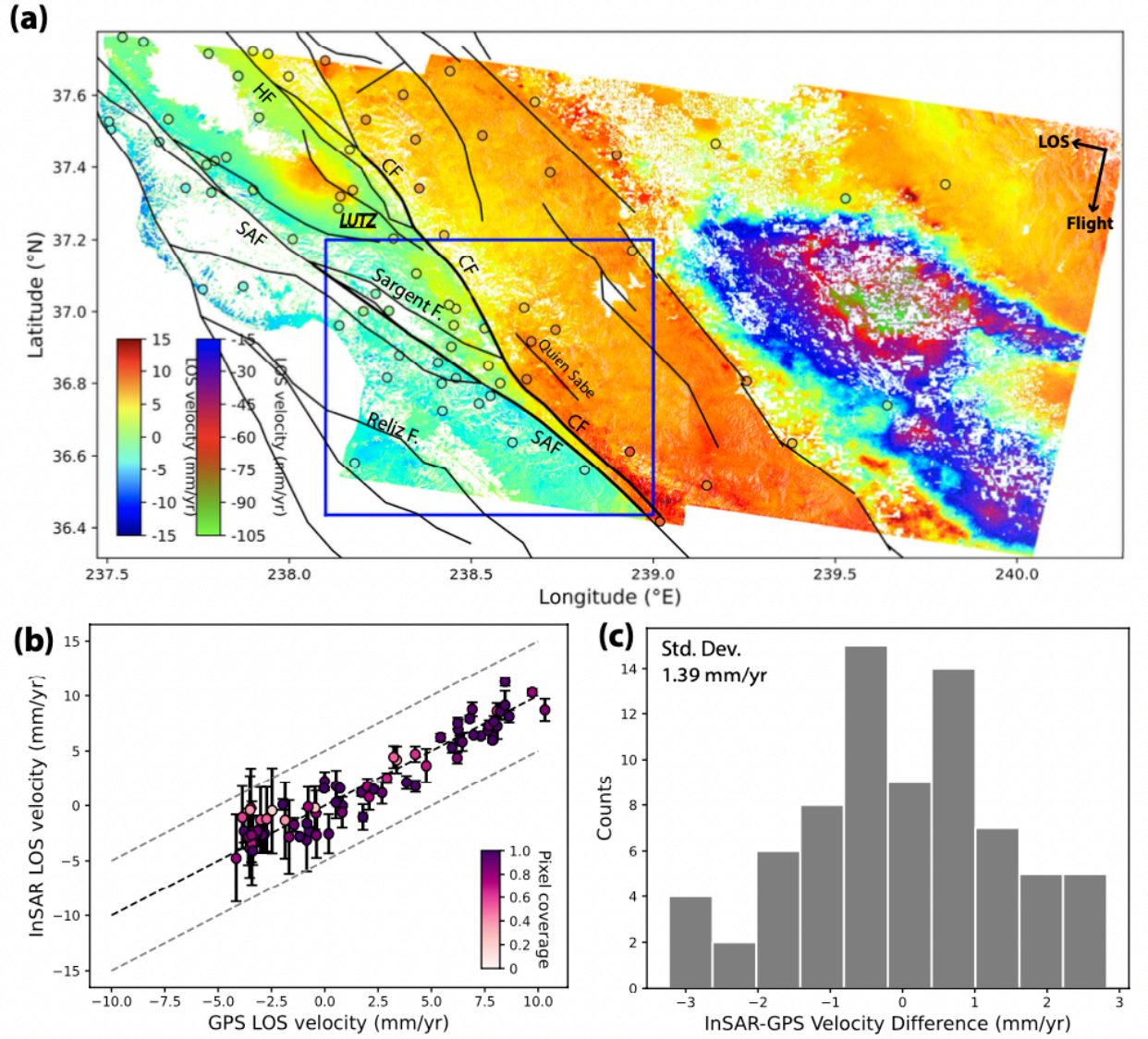

Figure 2 InSAR results and validation with GPS velocities. (a) Average 2015-2020 LOS velocity map for descending track 42. Red color indicates motion towards the satellite and blue color indicates motion away from the satellite with respect to GPS station LUTZ. Colored circles show GPS LOS velocities projected from 3D velocities estimated from the GPS timeseries during the same time period. InSAR and GPS LOS velocities are in the same color scale. Blue rectangle outlines the SAF-CF junction shown in Figure 3a. (b) Comparison of the InSAR and GPS LOS velocities. Stations within the Central Valley are excluded (Table S2). (c) Histogram of the InSAR-GPS velocity differences with

a standard deviation of 1.39 mm/yr.

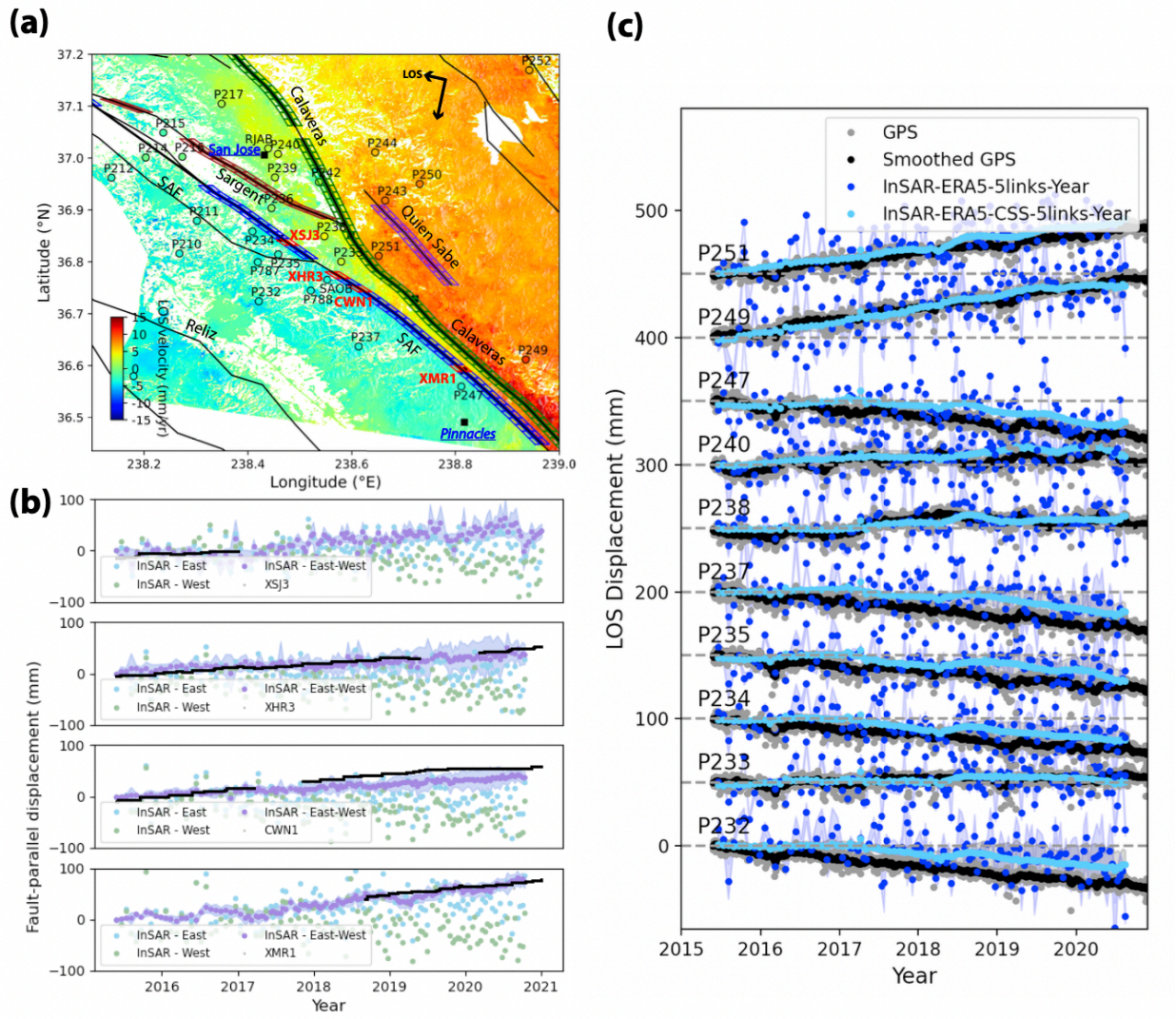

Figure 3 InSAR time series and validation. (a) Close-up view of the secular velocity field in the SAF-CF junction outlined in Figure 2a. Locations of near-fault profiles on each side of the SAF, CF, SF and QSF are shown in blue, green, brown, and purple boxes. (b) Comparison of InSAR timeseries with 3D continuous GPS timeseries relative to station LUTZ. Locations of selected stations are shown in (a). Gray dots show the raw GPS timeseries, black dots show the smoothed GPS timeseries using a 14-day moving average, blue dots show the InSAR timeseries with ERA5 weather model correction, and cyan dots show the InSAR timeseries corrected with both the ERA5 weather model and common scene stacking method (Tymofyeyeva et al., 2015). (c) Comparison of

cross-fault slip inferred from InSAR timeseries (purple) with creepmeter data (black), assuming fault-parallel strike slip. The InSAR cross-fault timeseries are derived by differencing InSAR timeseries averaged in cross-fault boxes (red boxes in (a)) east (light blue) and west (light green) of the fault.

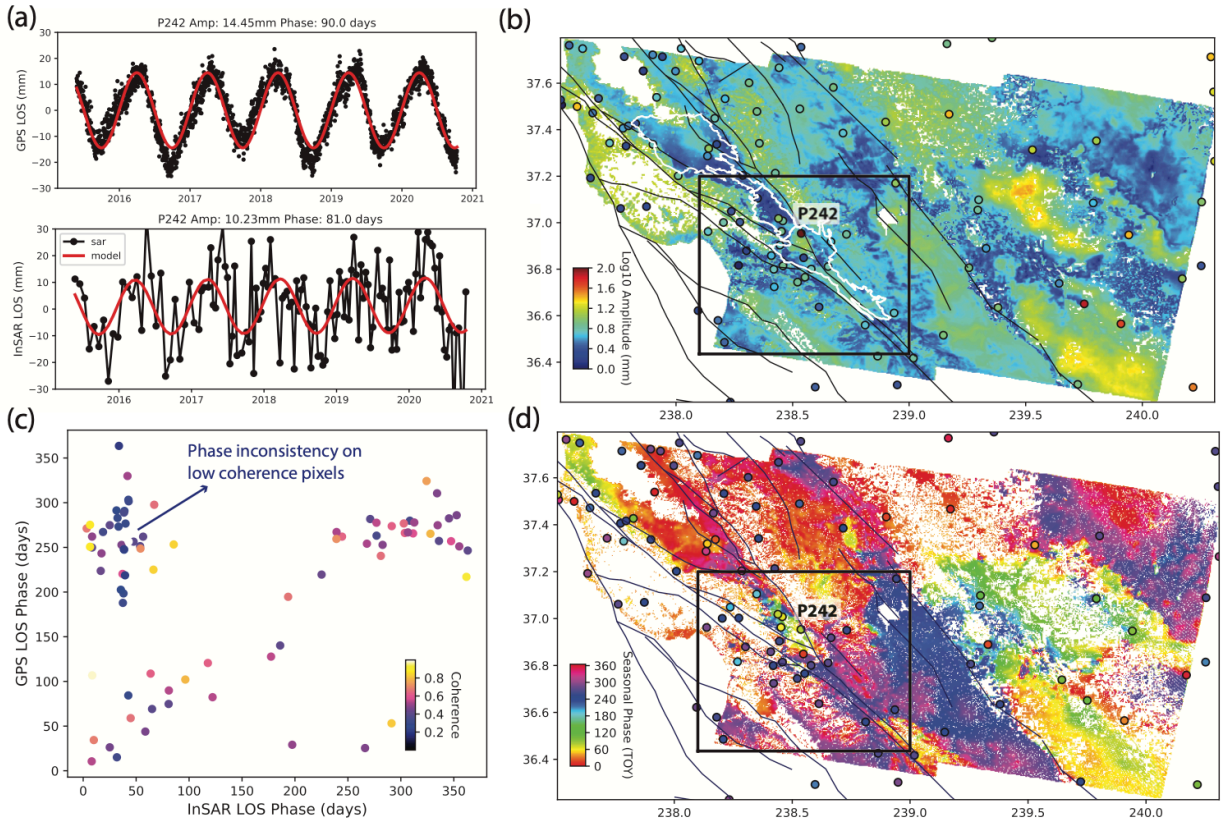

Figure 4 Evaluation of the timing of peak seasonal uplift (phase) from InSAR and LOS GPS timeseries in a North American reference frame. (a) Example of InSAR and GPS timeseries at station P242. Best-fitting seasonal sinusoidal functions are shown in red curves. (b) Amplitude and (d) timing of peak seasonal uplift (phase) map obtained from InSAR timeseries. The seasonal amplitude is shown in log scale. No phase is computed if estimated amplitude is 3 mm. Amplitude and phase values derived from GPS timeseries are shown in colored circles. Black rectangle outlines the SAF-CF junction, and white lines in (b) delineate young sedimentary basins in the vicinity of the SAF and CF faults (see Figure S7 for basin depths across the area). (c) Comparison of timing of seasonal uplift from InSAR and GPS timeseries. Each dot is colored with the average coherence from InSAR.

Figure 4 b and d show the seasonal amplitude and phase maps derived from the InSAR and GPS timeseries in the North American reference frame. A phase

of peak uplift in early spring is consistent with the poroelastic response to aquifer recharge at local groundwater basins (e.g. San Benito-Hollister Basin), whereas a peak in late summer and autumn suggests contributions of the elastic unloading response to the reduction in total water storage in the dry season (e.g. Amos et al., 2014).

$$\mathbf{disp} = \mathbf{A}\sin(\ t) + \mathbf{B}\cos(\ \mathbf{t}) + \mathbf{C}\sin(\mathbf{2}\ t) + \mathbf{D}\cos(\ \mathbf{t}) + \mathbf{Et} + \mathbf{F} \quad \textit{(Eq 7)}$$

$$\textit{annual amplitude} = \sqrt{\mathbf{A^2} + \mathbf{B^2}} \quad \textit{(Eq 8)}$$

$$\textit{annual phase} = \tan^{-\mathbf{1}}\frac{\mathbf{A}}{\mathbf{B}} \quad \textit{(Eq 9)}$$

The phase derived from InSAR and GPS timeseries agrees well, especially for pixels with coherence >0.2 (Figure 4c). The phase inconsistency mainly occurs for low-coherence pixels, and the InSAR phase clustered at ~50 days is likely due to unmodeled residual atmospheric noise. Figure S10 shows the standard deviation of residual timeseries after subtracting the best-fitting model (Eq 7), where we observe residuals increase with distance away from the reference station LUTZ, as well as in InSAR low coherence areas.

3.2 Spatial distribution of average creep rates along South Bay Area faults

We measure the spatial distribution of surface creep rates along the South Bay Area faults (the SAF, CF, SF and QSF). To achieve this, we take InSAR timeseries averaged from 1-km-wide, 1-km-long boxes 0.5 km to 1.5 km on each side of the fault and use the cross-fault timeseries differences to obtain the LOS-displacement timeseries of shallow fault creep. Locations of the cross-fault boxes are shown in Figure 3a. The profile length is selected to be 0.5-1.5 km on each side of the fault following our previous work (Li & Bürgmann., 2021), and more detailed discussion on the effect of profile length on creep rate estimation can be found in Li & Bürgmann (2021). Given that atmospheric noise is dominantly a long-wavelength signal in space (Bekaert et al., 2015), nearby pixels share common atmospheric noise features and the majority of atmospheric noise can be canceled out by taking the cross-fault differences. The atmospheric perturbation is significantly reduced after differencing the timeseries (Figure 3c). Figure 5 shows the LOS displacement timeseries along the two faults arranged by latitude. For each InSAR cross-fault displacement timeseries, we estimate the average creep rate through linear regression, and evaluate the residual displacement timeseries as a representation of short-term creep rate variation (Figure 5c). In this section, we only discuss the spatial distribution of average fault creep rates along those faults and will consider the residual timeseries (Figure 7) in Section 3.3.

The spatial distribution of the average surface creep rate along the SAF and CF is shown in Figure 6. Assuming insignificant vertical fault displacements in the region, the LOS creep rate is converted to the right-lateral rate (Eq 10), where $[\mathbf{l_e}, \mathbf{l_n}]$ are the horizontal components of the look vector and is the fault strike. A detailed list of the derived creep rates is shown in Table S3. At the SAF-CF junction, the SAF is transitioning from its central creeping section to the locked

Santa Cruz Mountain segment that hosted the 1989 Loma Prieta earthquake. The creep signal is clearly defined by sharp LOS velocity discontinuities along both the SAF and CF (Figure 2a). Our InSAR observations clearly document the existence of shallow fault creep on the subparallel sections of the SAF and CF, where the faults extend for about 50 km with only <5 km separation. Our results capture the decrease in surface creep rate along the SAF from ~18 mm/yr near Pinnacles/Dry Lake Valley to fully locked north of San Juan Bautista. The CF steps from the SAF at ~36.4°N, accommodates a portion of the tectonic motion of the San Andreas Fault system and also exhibits fault creep. The inferred strike-slip creep rate on the CF increases from ~10 mm/yr in the south and reaches its peak rate of ~20 mm/yr at 36.9°N. Along the subparallel section (36.4°N-36.7°N), the northward decrease of the SAF creep rates is accompanied by an increase of CF creep rates. This anticorrelated distribution of creep rates possibly indicates shallow slip partitioning between the two faults (Figure 6a).

$$\mathrm{CR}_{\mathbf{right-lateral}} = \frac{\mathrm{CR}_{\mathrm{LOS}}}{[\mathbf{l_e}, \mathbf{l_n}] \bullet [\sin\ , \cos\ ]} \quad \textit{(Eq 10)}$$

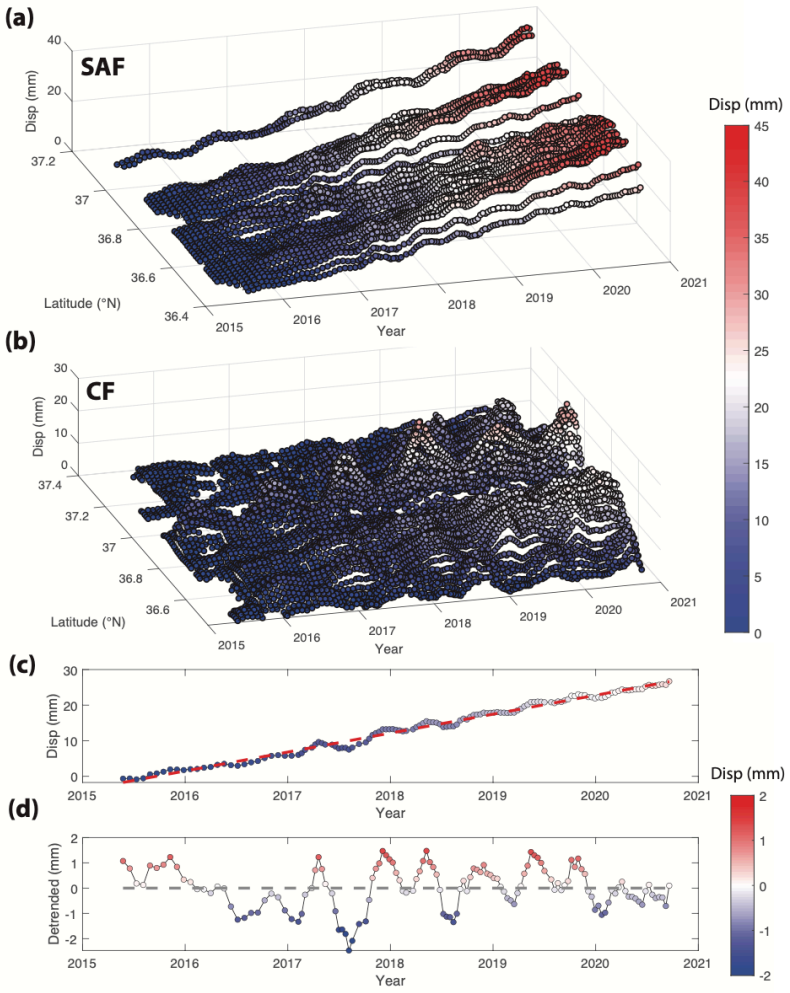

Figure 5. Cross-fault timeseries differences along the (a) SAF and (b) CF. The cross-fault timeseries are calculated by differencing the InSAR timeseries averaged from 1-km-wide, 1-km-long boxes 0.5-1.5 km on each side of the faults (Figure 3). (c) Example of cross-fault timeseries on the SAF at latitude 36.45 °N. The average InSAR LOS rate due to fault creep is estimated by linear regression (red dashed line). (d) we subtract the average creep rate from the original timeseries to highlight the short-term rate variations in the LOS direction. Short-term rate variations after removing the average rate on all profiles are shown in Figure 7.

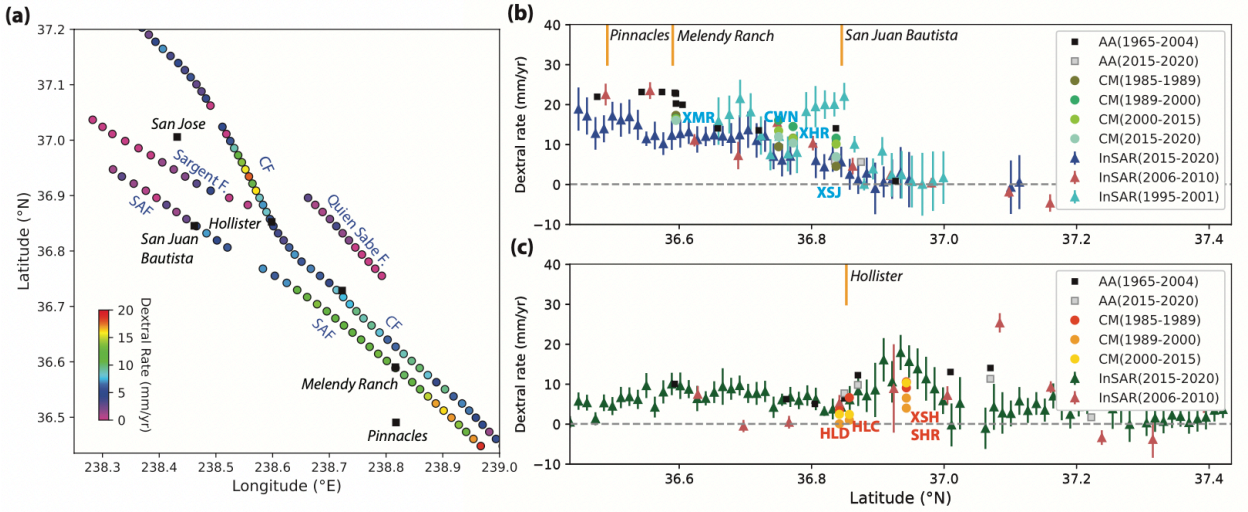

Figure 6 (a) Spatial distribution of average creep rate derived from cross-fault timeseries differences along the SAF, CF, SF and QSF (Table S3) in map view. Spatial distributions of average right-lateral creep rates along the (b) SAF and (c) CF arranged by latitude. We convert the InSAR LOS rate to right-lateral creep rate assuming all LOS motions are from horizontal fault-parallel fault creep. Blue and green triangles show the creep rates derived in this study (2015-2020) on the SAF and CF, respectively. Cyan and pink triangles show the results from InSAR during 1995-2001 (Johanson & Bürgmann, 2005) and 2006-2010 (Tong et al., 2013), respectively. Green and orange dots with different shades show the rates from creepmeter measurements during 1985-1989 (pre-Loma Prieta earthquake), 1989-2000 (post-earthquake), 2000-2015, 2015-2020, respectively. Black and gray squares show measurements from alignment arrays from multiple sources spanning 1965-2004 and 2015-2020 (McFarland et al, 2017) (Table S4).

We cross-validate our Sentinel-1 InSAR derived creep rates (2015-2020) on the SAF and CF with existing geodetic measurements, including previous InSAR (ERS, 1995-2001, Johanson & Bürgmann, 2005; ALOS, 2006-2010, Tong et al., 2013), alignment arrays (1965-2004, e.g. Burford & Harsh, 1980; Lisowski & Prescott, 1981; Galehouse & Lienkaemper, 2003; Titus et al., 2006) and creepmeter measurements (1985-2020, e.g.Bokelmann & Kovach, 2003; Bilham et al., 2004) (Figure 6b, c). A detailed record of the derived creep rates from other sources is listed in Table S4. Overall, our InSAR-derived creep rates are consistent with the previous datasets. However, we find the surface creep rate derived from ERS InSAR (1995-2001) is significantly higher along a 10-km-long section just south of San Juan Bautista (~36.8°N), compared to that derived from ALOS (2006-2010) and Sentinel-1 (2015-2020) data (Figure 6b). Behr et al. (1990) and Bokelmann & Kovach (2003) observed accelerated surface creep rates on the San Juan Bautista section of the SAF in response to the 1989 Loma Prieta earth-

quake, and such accelerated creep is also indicated by repeating earthquakes in the region (Turner et al., 2013). The higher creep rates during 1995-2001 may be due to the lingering effect of the fault's response to the 1989 Loma Prieta earthquake and its enduring, deep seated viscoelastic relaxation (Huang et al., 2016). The overall consistency between pre-1989 measurements and present-day InSAR measurements indicates the creep activity has mostly returned to pre-earthquake levels.

We also estimate the shallow creep along the SF and QSF with the same approach we applied to the SAF and CF (Figure 6a). The InSAR cross-fault timeseries differences are shown in Figure S11, S12 for the SF and QSF, respectively. We identify a section that creeps at up to 4.2±3.1 mm/yr on the SF, while the other section of the fault appears fully locked (Figure 6a). Additionally, surface creep up to 3.5±2.6 mm/yr is identified along the QSF. Regardless of the substantial uncertainties on the creep rate estimation, we can at least provide an upper bound of surface creep rates along the SF and QSF from the noisy InSAR timeseries. A detailed documentation of the InSAR-derived creep rates on all faults is provided in Table S3.

3.3 Spatiotemporal variation of the short-term creep rates along the SAF and CF

To capture the time-dependent characteristics of the deformation, we subtract the 2015-2020 linear trend from the InSAR timeseries and focus on the residual InSAR timeseries as representing the displacement history that deviates from the long-term trend (Figure 5c). Figure 7a, b shows the spatiotemporal variation of the residual InSAR timeseries, representing short-term LOS displacement deviations along the SAF and CF. The InSAR timeseries are resampled into 12-day intervals to accommodate less frequent radar acquisition before the launch of Sentinel-1B in 2016. We also use a 60-day by 10-km-distance moving average window to smooth the spatiotemporal timeseries. Even though no significant vertical rates are indicated near the fault based on the GPS velocities (<2 mm/yr, Figure 1), seasonal deformation, mostly contributed by vertical hydrological loading, still dominates some of the residual timeseries (e.g., Figure 7c-A). We divide the cross-fault timeseries into segments, defined by their dominant timing of maximum seasonal LOS variations, and stack-averaged the residual timeseries in each segment (Figure 7c). North of 36.9°N, the InSAR timeseries with strong seasonal displacements matches well with the vertical timeseries from a nearby GPS station, P242. Further to the south between 36.4°N-36.7°N, we see phase-shifted timing of the seasonal cycles along the SAF and CF.

Variable timing of maximum seasonal uplift inferred from the InSAR timeseries has been discussed in Section 3.1 (Figure 4), where the phase representing the seasonal trough in the LOS timeseries (consistent with peak uplift) in early Spring can be related to the poroelastic response of aquifer systems to groundwater-level rise, and the phase in late summer is consistent with the elastic response to California's water loading cycle. This could also explain

the distinct seasonal cycles of the InSAR cross-fault timeseries along different segments, where the two sides of the fault may be exposed to different deformation processes (e.g., Figure 7c-D). According to the sediment thickness map from Shah & Boyd (2018, Figure S13) and our InSAR phase analysis, thick sediments in the Hollister-San Benito basin between the SAF and CF exhibit poroelastic deformation associated with groundwater-level changes in a confined aquifer. This is likely the main cause of the seasonal cycles in the cross-fault InSAR timeseries, leading to anticorrelated patterns in the cross-fault residual timeseries observed on the SAF and CF. Therefore, we attribute most, if not all of the short-term deformation observed in the cross-fault InSAR LOS timeseries to contributions from vertical hydrological deformation processes, rather than a tectonic source.

To minimize the effect of short-term seasonal contributions from hydrological deformation processes on the estimated fault creep, we apply an 18-month low pass filter to the residual InSAR timeseries. The low-pass filtered spatiotemporal distribution of fault creep is shown in Figure 7 d,e,f. The 18-month window is selected to ensure the seasonal signals are effectively removed. We observe multi-year long-term creep rate changes (deviating by up to 2-3 mm from the long-term average rates) along the SAF and CF from the low-passed filtered InSAR timeseries. We see a rate decrease around mid-2017 on both the SAF and CF, mostly between 36.5°N-37.5°N, where the two faults are sub-parallel to each other with <5 km separation. We will validate the observed subtle coupling change with information from seismicity and CREs in section 4.3.

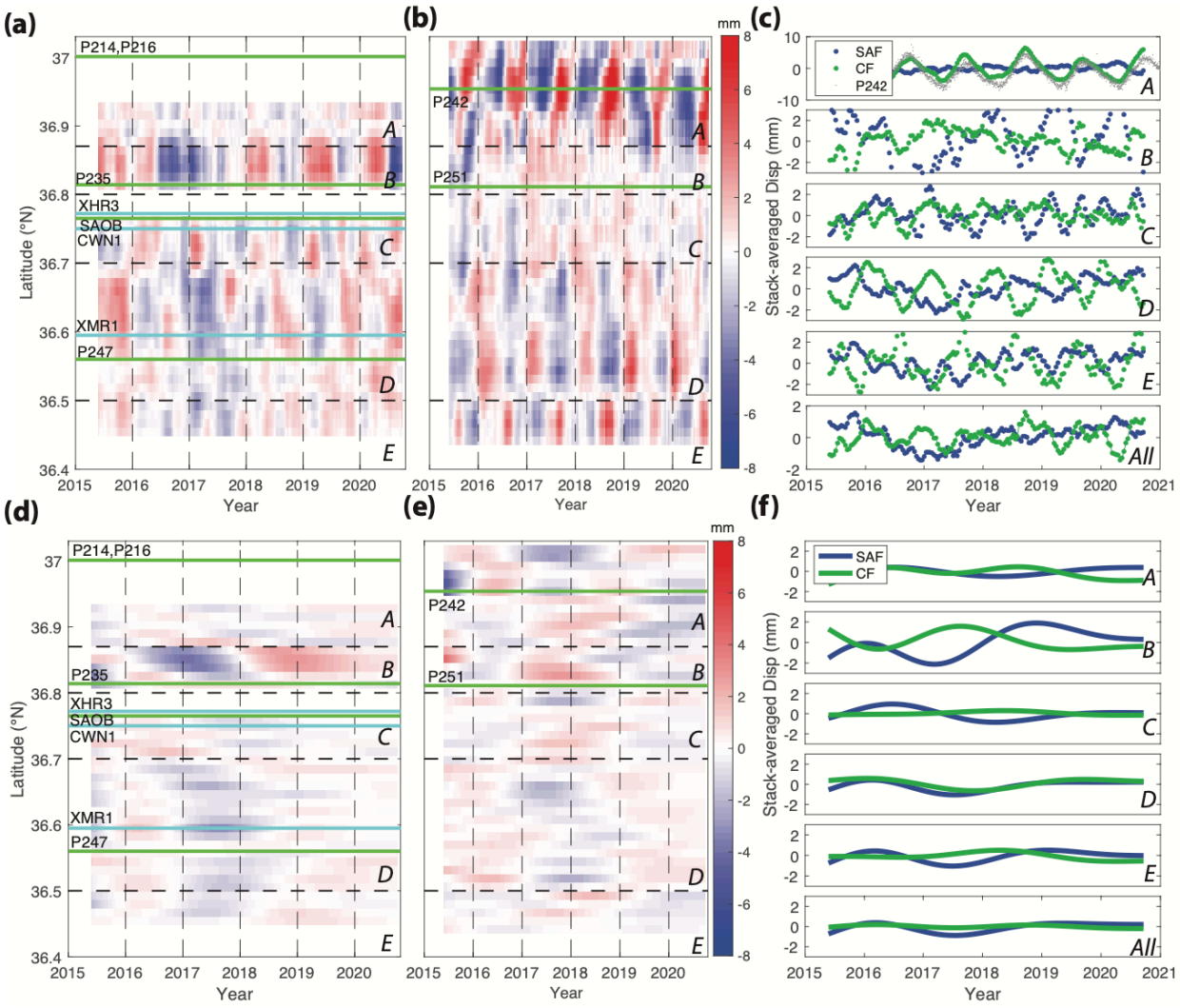

Figure 7 Spatiotemporal variation of the residual InSAR timeseries after the removal of a linear trend across the (a) SAF and (b) CF. The red color indicates periods when the short-term displacement exceeds the long-term trend, whereas the blue color indicates short-term displacement below the long-term trend (see Figure 5). The locations of near-fault GPS and creepmeter sites are shown with labeled green and cyan lines, respectively. (c) Stack-averaged residual InSAR timeseries for the corresponding fault segments A through E arranged by latitude for both SAF (blue) and CF (green). The fault segmentation is indicated with black dashed lines in (a) and (b). (d) Multi-annual variation of the residual InSAR timeseries on the SAF after applying an 18-month low-pass filter on (a). (e) Multi-annual variation of the residual InSAR timeseries on the

CF after applying an 18-month low-pass filter on (b). (f) Stack-averaged residual InSAR timeseries on each fault segment after 18-month low-pass filtering. The blue and green lines show the timeseries on the SAF and CF, respectively.

3.4 Spatiotemporal variation of the b-value at the SAF-CF junction

We estimate the spatiotemporal distribution of the b-value at the SAF-CF junction using the declustered and relocated catalog from NCEDC (1984-2021) (Waldhauser & Schaff, 2008; Waldhauser, 2009). The spatial distribution of the seismicity and the resolved b-values calculated in 0.05° grid elements around the SAF-CF junction are shown in Figure 8a. For each grid cell, we extract all available events during 1984-2020 within the grid, and only estimate b-values for grid cells containing N>200 events. Then, we estimate the magnitude of completeness $\mathbf{M_c}$, and obtain the a-value and b-value using Eq 4 on all valid grids. The spatial distribution of $\mathbf{M_c}$, a-value and b-value uncertainties are shown in Figure S14. To examine the effect of clustered seismicity on the b-value estimation, we compare the spatial distribution of seismicity and b-value before and after declustering, finding a very similar spatial pattern (Figure S15). The SAF generally has a lower b-value (0.4-0.8) than the nearby CF (0.8-1.2) derived from both original and declustered catalogs.

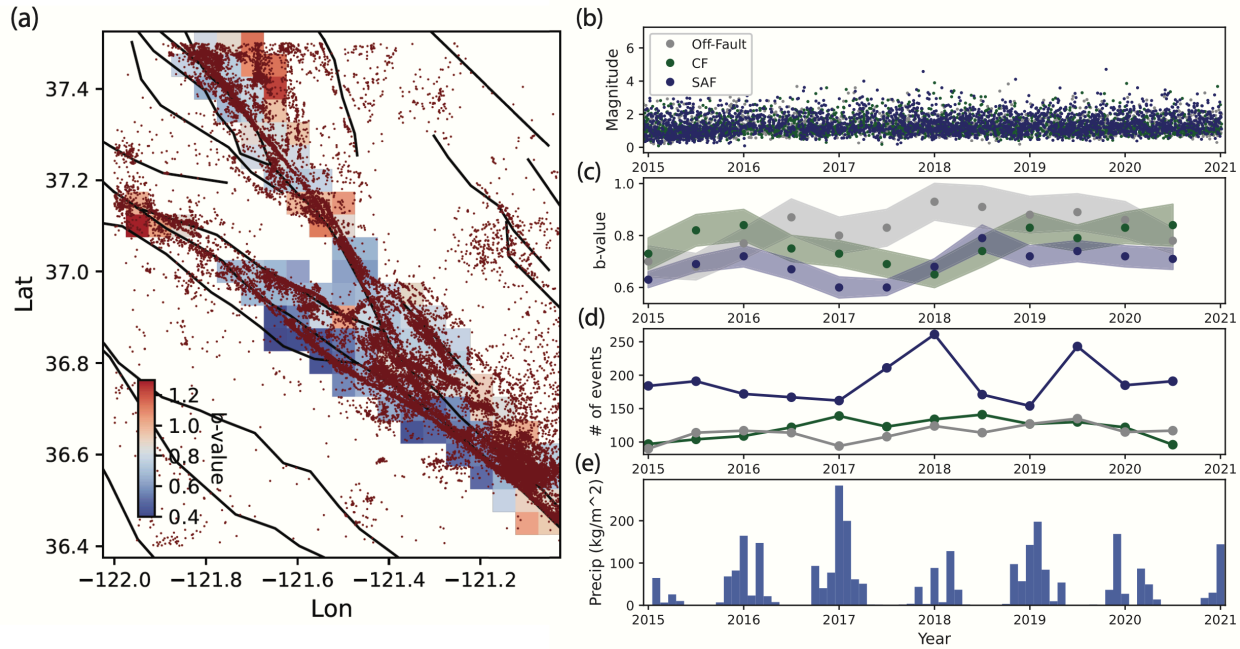

Figure 8 (a) Spatial distribution of the double-difference relocated and declustered seismicity from NCEDC (1984-2021) and b-values in the study region. (b) Magnitude-time plot of the declustered seismicity (2015-2020) along the SAF, CF and off-fault events. (c) Temporal evolution of b-values calculated with a 1-year moving window that steps by 0.5-year for each seismicity group (see (b)

for color legend). (d) The total number of M>Mc events in each time interval for each seismicity group. (e) Monthly total precipitation in the study area retrieved from NLDAS (Xia et al., 2012).

We inspect the temporal variation of the b-value during 2015-2020, corresponding to the InSAR observation period in this study. Limited by the total number of available events in each time interval, we use a 1-year moving window (±0.5 year) window with 0.5-year step to ensure at least 100 events in each time step (Figure 8). We then separate the microseismicity into three groups, including the seismicity along the SAF and CF within 2.5 km of the fault traces, and off-fault events that are >2.5 km away from the two faults. The total number of events in each time step and the resolved b-values along the SAF, CF and off-fault areas are shown in Figure 8c,d,e. Monthly precipitation data from the North America Land Data Assimilation System (NLDAS, Xia et al., 2012) is shown in Figure 8f. The b-values fluctuate along the SAF and CF, whereas they are more stable in the off-fault region. The b-values decrease between 2016-2017 and recover between 2017-2018, leading to relatively low b-values in 2017 along the SAF and CF. The temporal changes of the b-values between 2016-2018 have a similar pattern as the long-term decrease of creep rate from the residual InSAR timeseries. In addition, we do not see a significant seismicity rate change during the period of b-value changes (Figure 8d). The potential mechanisms underlying the b-value variations in 2016-2018 and their correlation with the InSAR long-term creep rate changes will be further discussed in Section 4.4.

4 Discussion

In this section, we will discuss the observed shallow fault creep on the SF and QSF (Section 4.1) and explore the partitioning of shallow fault creep between the SAF, CF, SF and QSF (Section 4.2). In the last section (Section 4.3), we relate the observed multi-year coupling change from InSAR timeseries to variations in CREs and seismicity, and propose possible driving mechanisms underlying the observations.

4.1 Shallow Fault Creep on the SF and QSF

Being one of the main faults in the area between the SAF and CF at the SAF-CF junction, the 55-km-long SF appears to connect the locked section of the SAF in the Santa Cruz Mountains and the creeping CF near Hollister (Figure 1, Mongovin & Philibosian, 2021). The southern SF has been shown to creep at the surface at 2.9±0.7 mm/yr (Prescott & Burford, 1976). A recent study by Mongovin & Philibosian (2021) resurveyed the alignment array sites of Prescott & Burford (1976) and obtains a creep rate of 3.3±1.3 mm/yr and 1.7±0.8 mm/yr for the northern and southern arrays, which are 3.7 km apart from each other. Evidence from repeating earthquake sequences suggests a 1-2 mm/yr (Turner et al., 2013) or 5.3±2.0 mm/yr (Waldhauser & Schaff, 2021) fault creep rate at 2.5-7.5 km depth on the SF. Similar to the creeping sections of the SAF and CF, there are CREs along a 20-km-long southern section of the SF (Turner et al., 2013; Waldhauser & Schaff, 2021; this study). The co-existence of InSAR-

observed shallow creep (up to 4.2±3.1 mm/yr) and CREs indicates that slow slip on the SF plays an important role in slip partitioning and strain transfer on the SAF system.

The 25-km-long QSF is located near the southeastern Hollister Valley, east of creeping sections of the SAF and CF. Unlike the localized seismicity observed along the SAF, CF, and SF, the seismicity is distributed across a 2-4 km wide zone (Watt et al., 2014). Based on CRE observations, the fault has been inferred to creep at depth at 2.2-11.4 mm/yr (Templeton et al., 2008b) and 5.4±2.0 mm/yr (Waldhauser & Schaff, 2021). Recent geological mapping also found en-échelon cracks on a fault-crossing road surface in the southern Hollister Valley section of the fault (Baldwin & Bloszies, 2022), indicating possible evidence of aseismic slip on the fault. Our InSAR results also indicate surface creep at up to 3.5±2.6 mm/yr.

Our work provides the first InSAR observation of shallow creep (0-4 mm/yr) along the SF and QSF, and the information on fault coupling from the geodetic and repeating-earthquake data should be of value for rupture-scenario simulations and seismic hazard analysis for these faults. This indicates that secondary structures, including the creeping SF and QSF, participate in the complex shallow deformation along the SAF-CF junction, accommodate more distributed deformation away from the two primary fault strands, and relieve some of the tectonic loading by continuous creep.

4.2 Partitioning of the shallow fault creep among the SAF and CF

At the SAF-CF junction, the SAF is transitioning from rapidly creeping at the surface to fully locked, while the CF branches from the SAF and exhibits spatially variable creep rates. Understanding how slip partitions among the main fault strands of the SAF system is crucial for seismic hazard evaluation (Field et al., 2014), especially in the densely populated Bay Area. A number of hypotheses have been proposed to explain the extent of fault creep, including the presence of frictionally weak and velocity-strengthening materials in the fault core (e.g. Lockner et al., 2011; Moore & Rymer, 2007), low effective normal stress due to elevated pore pressure (e.g. Wei et al., 2009) and faults that have high roughness and complex fault structure (Bürgmann, 2018). Fault geometry has also been proposed to be a key factor controlling the spatial distribution of fault creep, including the local fault strike with respect to the regional principal stress orientations (Jolivet et al., 2013), creep locatization on transpressional segments (Bilham & Williams, 1985; Lindsey et al., 2014), and fault roughness that possibly leads to a heterogeneous stress field and promotes creep (Jolivet et al., 2015).

Here we explore the correlation of fault creep with the local fault geometry, specifically the angle between fault strike and background stress orientation (Jolivet et al., 2013). The regional background stress orientation resolved from M>1.5 focal mechanisms (Johnson et al., 2017) is shown in Figure 9. Despite some variations, the background stress orientation remains mostly uni-

form across the study region. We take N15°E as the maximum horizontal stress orientation (in Eq 11), assuming a uniform background stress in the SAF-CF junction. We then calculate the proportion of the maximum principal stress that is projected onto the receiving fault geometry. That is, assuming a uniform background stress field and loading rate, the proportion of stress that is effectively acting in the fault-parallel (shear) and perpendicular (normal) directions on the local fault geometry. We refer to these measures as the unit shear- and normal-stress loading rates along the SAF and CF (Figure 9, Eq 11, 12), where is the local fault strike and is the maximum horizontal stress orientation.

$$\dot{} = \cos(\mathbf{2}(-)) \quad \textit{(Eq 11)}$$

$$\dot{} = \sin(\mathbf{2}(-)) \quad \textit{(Eq 12)}$$

The spatial distribution of creep rate and the unit shear- and normal-stress loading rates are shown in Figure 9. We further assess the variation of normalized creep rate and the normal- and shear-stress loading rates on the SAF and CF arranged by latitude (Figure 10). For the SAF, a striking correlation between the creep rate and relative shear stress loading (r=0.74), and anticorrelation with normal-stress loading (clamping) are observed (r=-0.71) (Figure 10a). Even though the correlation for the CF is less clear (Figure 10b), the distribution of fault creep still matches the stress loading patterns to the first order. Particularly at ~36.9°N on the CF, the peak creep rates match the location with high shear stress and low normal stress. This correlation suggests that the fault geometry, and thus the local shear- and normal-stress loading on the fault plane, play a role in controlling the first-order variation of surface creep rates.

Our results show that creep rate variations may be influenced by geometry and effective normal stress, where higher shear-stress and lower normal stress loading rates tend to promote aseismic fault creep at the SAF-CF junction. This is opposite to the observation on the southern SAF (Bilham & Williams, 1985; Lindsey et al., 2014), where higher rates of localized creep are more evident on transpressional segments. The possible effect of fault-normal convergence rates on fault creep has also been discussed by Argus & Gordon (2001), who found that reduced fault-normal convergence rates can only partially explain the distribution of creeping faults along the SAF system. That is, even though there is overall support for the hypothesis that low fault-normal convergence rates and stress are associated with stable fault creep, there are also counter examples. What we observe at the SAF-CF junction and the observations along the southern SAF (Lindsey et al., 2014), may represent end-member cases of the hypothesis discussed by Argus & Gordon (2001).

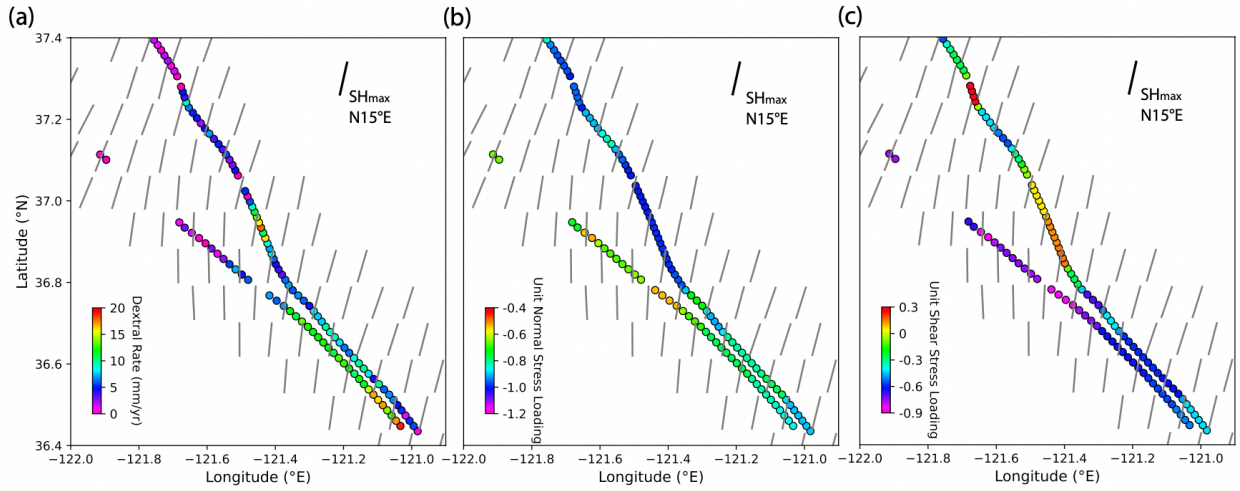

Figure 9 Map view of the spatial distribution of (a) creep rates, (b) unit normal-, and (c) shear stress loading rate on SAF and CF. The unit normal and shear stressing loading rates are calculated assuming an average N15°E maximum horizontal stress orientation. Background maximum-stress orientations in the study region are from Johnson et al. (2017). Positive unit normal stress loading rate indicates clamping while negative value indicates unclamping.

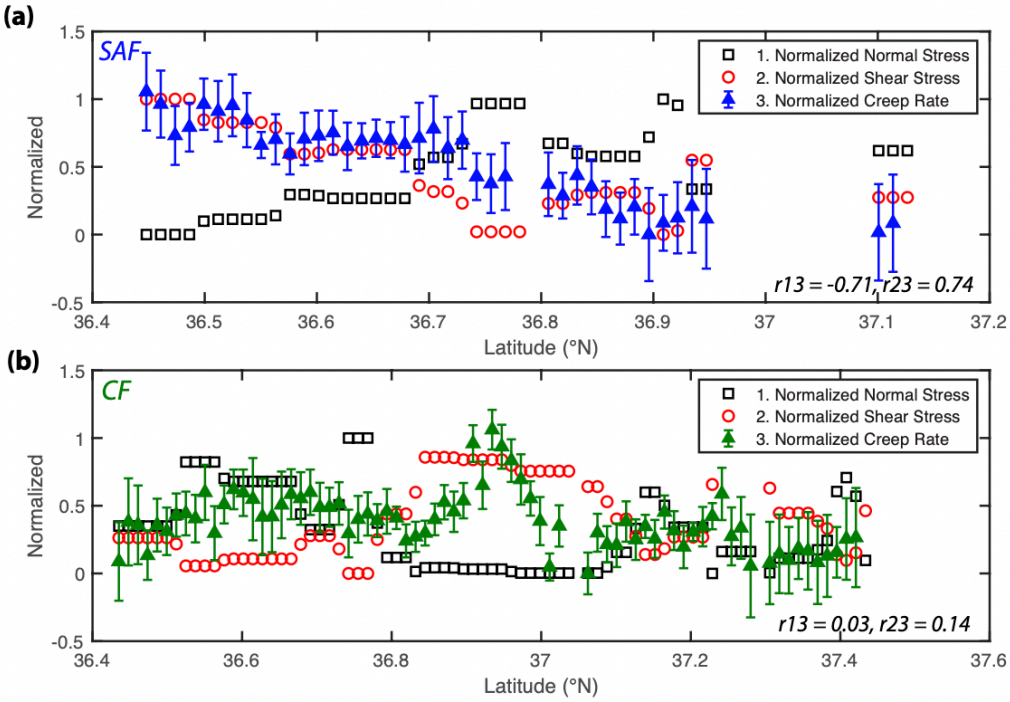

Figure 10 Spatial distribution of normalized creep rate, normal and shear stress loading on the (a) SAF and (b) CF arranged by latitude. The background maximum horizontal stress orientation is assumed to be N15°E. Larger normal stress loading rate indicates more clamping while smaller indicates reduced clamping. The correlations between normalized stress components and creep rate are labeled in the plot (subscript number pairs refer to numbered values in legend), where r=-1 indicates anti-correlation and r=1 indicates perfect correlation.

At the SAF-CF junction, the tectonic loading of the SAF system is mainly accommodated by the SAF and CF. Secondary structures like the SF and QSF also play a role in the partitioning. If there are multiple faults that are weakly coupled, it is likely that creep gets distributed among them to continually relieve the tectonic loading. To explore the spatial partitioning of shallow fault creep among the SAF, CF, and secondary structures, we project the creep rates onto a profile parallel to the creeping section of the SAF (N45°W) and calculate the summed creep rates among all faults (Figure 11). The along-fault sum of right-lateral creep rates remains steady (~20-25 mm/yr) from 0-60 km along-fault distance from Bitterwater (121°W, 36.4°N), where the SAF and southern CF are subparallel to each other. The summed creep rates gradually decrease northward (60-100 km distance), where the fault creep is partially partitioned onto the SF and QSF (Figure 11b). Further to the north, a further decrease of the summed creep rates is indicated, as most of the CF creep is transferred to the Hayward Fault (Chaussard et al., 2015).

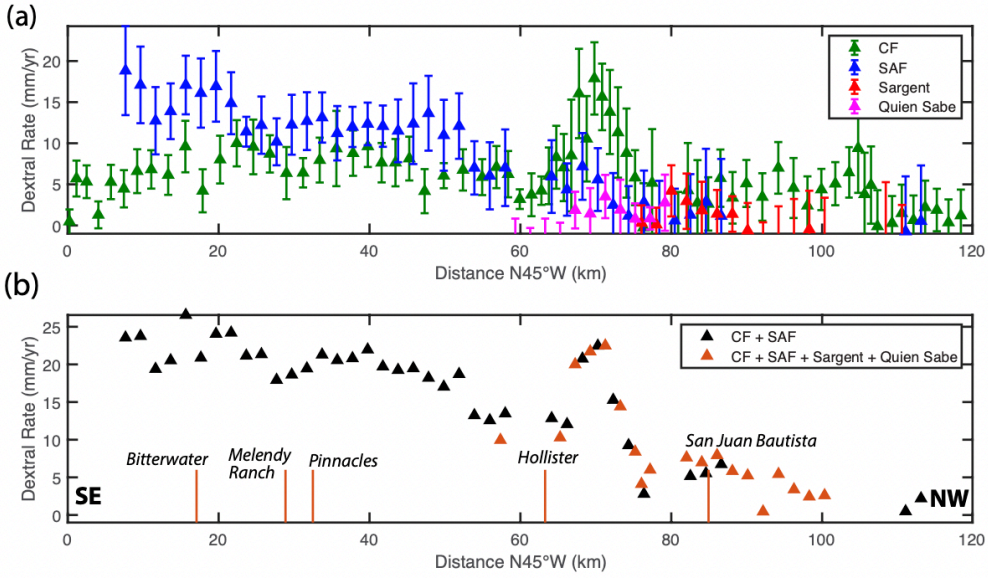

Figure 11 (a) Along-fault (N45°W) distribution of creep rates on the SAF, CF, SF and QSF. (b) Along-fault sum of right-lateral creep rates on the SAF, CF, SF and QSF. The along-fault distance is calculated with respect to Bitterwater

(121°W, 36.4°N).

We show that the shallow aseismic slip can be partitioned between nearby structures simply due to geometric constraints. Of course, other factors also affect the distribution of shallow creep rate, such as fault frictional properties (e.g. Jolivet et al., 2013) and the spatial distribution of locked asperities at depth (e.g., Savage & Lisowski, 1993; Bürgmann et al., 2000; Simpson et al., 2001). The absolute differences of the tectonic loading projected on fault sections due to variable fault strike are quite subtle. The modulation of fault creep by stress loading may thus indicate relatively low frictional resistance of the creeping faults in the SAF system, particularly for the SAF. Such low friction on the creeping section of the SAF has also been supported by stress orientations (Provost & Houston, 2001), heat flow measurements (d'Alessio et al., 2006), and laboratory experiments (Lockner et al., 2011).

4.3 Long-term coupling changes along the SAF and CF

As described in Section 3.3, we see a subtle, multi-year change of the long-term creep rate along the SAF and CF after applying an 18-month low-pass filter on the original detrended InSAR timeseries (Figure 7). To further investigate this feature, we compare the temporal variations of our InSAR-derived creep rates with slip inferred from CREs and changes in b-value derived from microseismicity in the study region during the same time period (2015-2020).

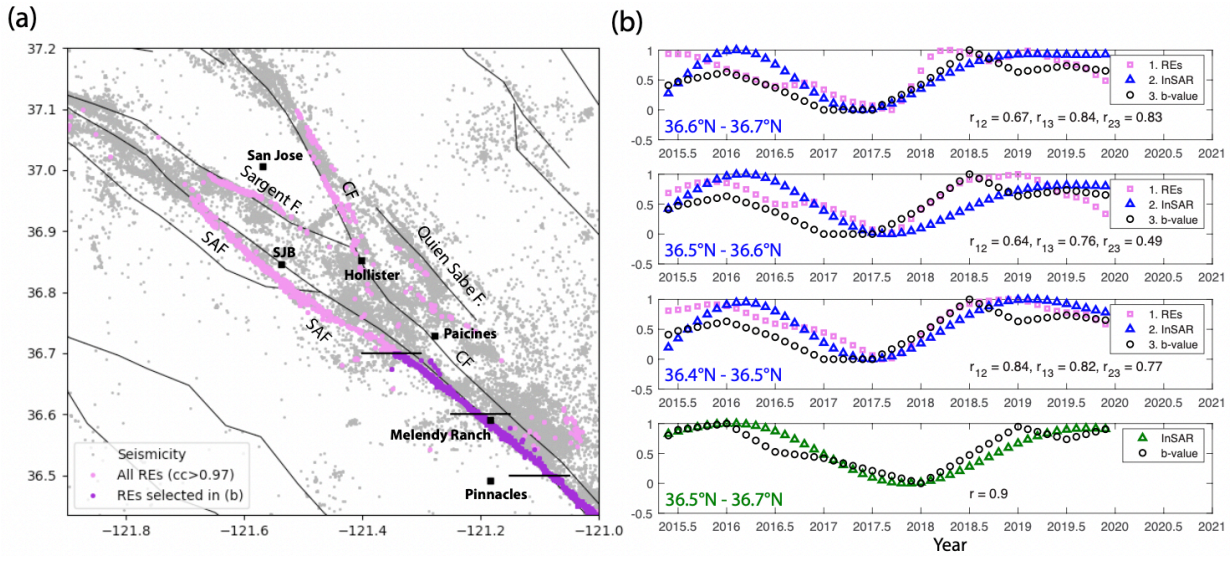

Figure 12 (a) Spatial distribution of the NCEDC seismicity (gray), repeating earthquakes with cc>0.97 (pink), and repeating earthquakes used to calculate the temporal variation of slip-rate change along the SAF in (b) (purple). (b) Temporal variation of b-value, residual slip timeseries inferred from InSAR and repeating earthquakes that are binned by latitude along the SAF and CF. Top

three panels show analysis on the SAF (blue) and bottom panel shows analysis on the CF (green). The residual InSAR, CRE-inferred slip and b-value timeseries are normalized to [0, 1]. The correlations between scaled b-value, residual InSAR and CRE-inferred slip timeseries are labeled in the plot (subscript number pairs refer to numbered values in legend).

The spatial distribution of the CREs is shown in Figure 12a. Following the same procedure previously applied to the InSAR timeseries, we remove a linear trend from the cumulative slip timeseries inferred from the CREs along the SAF and focus on the residual timeseries. The spatiotemporal variation of the residual slip inferred from CREs is shown in Figure S16. We only calculate the CREs inferred slip on the SAF because there are very few CREs on the CF (Figure 12a). A direct comparison of the temporal evolution of b-value, InSAR, and CRE-inferred creep rate on the SAF is shown in Figure 12b. Note that we normalized the b-value, InSAR, and CRE-inferred residual timeseries by their maximum values, given these measures cannot be directly compared with an absolute scale. During 2015-2020, we find similar temporal behaviors in the residual timeseries from both InSAR and CREs, indicating a lower than average rise in cumulative fault slip, particularly during Jan-June 2017. The residual timeseries gradually recover to the average level after reaching a minimum in June 2017. The same temporal pattern is also observed in the b-value variations along the SAF. The high correlation coefficient between all curves (0.68-0.84) lends support to the temporal coupling changes inferred from the low-pass filtered InSAR timeseries.

For the CF, we can compare the temporal evolution of b-value and residual InSAR (Figure 12b, bottom panel) due to the lack of repeating earthquake sequences on the CF. A high correlation coefficient (0.90) between the b-value and residual InSAR timeseries shows a lower than average rise in creep rate accompanied by a decrease in b-value, during 2017-2018. The temporal behavior of the b-values and residual InSAR timeseries on the SAF precede the CF by three to six months, indicating a possible transfer of slip at the SAF-CF with a time-lag.

A link between temporal b-value and creep rate changes has been discussed in Schorlemmer et al. (2004), where they find significant correlation between b-value change and a creep episode along the Parkfield section of the SAF in 1993. Our analysis suggests the correlation between long-term changes of b-value and residual deep and shallow slip inferred from CREs and InSAR timeseries for the SAF and CF fault section between 36.4°N-36.7°N. Assuming the tectonic loading remains constant over a longer period, a slight decrease of the deep slip rate suggests that temporarily less stress is released through seismic and aseismic slip, leading to increased stress levels, possibly reflected in lower b-values, which may indicate relatively higher seismic potential. The origin of such short-term, transient coupling changes could be due to temporal changes of fault frictional properties, variations of pore fluid pressure, fault zone damage, and dilatancy changes. It is worth mentioning that 2017 is a wet year with extensive precipitation (Figure 8e), the coupling change may between 2016-2018 is possibly

to be affected by the rainfall. Overall, all observations provide evidence of resolvable coupling changes between 2016-2018. The correlation of b-value and slip rate changes may indicate that the SAF and CF are sensitive to small stress perturbations. This also indicates that InSAR could be a promising tool for monitoring subtle spatiotemporal changes of coupling and stress conditions.

5 Conclusions

We perform a timeseries analysis using 5 years of Sentinel-1 InSAR data from May 2015 to October 2020 covering the southern San Francisco Bay Area. The derived InSAR velocities agree with the GPS LOS velocities with 1.39 mm/yr standard deviation for 66 stations, and the InSAR timeseries agree with GPS and creepmeter timeseries with 4.1 mm and 11.3 mm standard deviation, respectively. Fault creep rates on the SAF decrease from ~18 mm/yr at Pinnacles to fully locked ~10 km north of San Juan Bautista. The inferred strike-slip creep rate on the CF increases from ~10 mm/yr in the south and reaches its peak rate ~20 mm/yr at 36.9°N. Our InSAR observations clearly document the existence of shallow fault creep on the subparallel sections of the SAF and CF, where the faults extend for about 50 km with only <5 km separation. Along the subparallel section (36.4°N-36.7°N), the northward decrease of the SAF creep rates is accompanied by an increase of CF creep rates, suggesting a transfer of shallow slip. We provide upper-bound estimates of surface creep of 4.2±3.1 mm/yr for the SF and 3.5±2.6 mm/yr for the QSF. We show that the distribution of fault creep is to first order controlled by the angle between fault strike and the background stress orientation. We further examine the spatiotemporal variation of the long-term creep rates and find a long-term coupling increase during 2016-2018 along the SAF and CF. A striking correlation (0.68-0.98) between long-term changes of b-values and residual aseismic slip timeseries inferred from CREs and InSAR timeseries is found along the sub-parallel sections of the SAF and CF between 36.4°N and 36.7°N. The temporal behavior of the b-values and residual InSAR timeseries on the SAF proceed the CF by three to six months, indicating the possible transfer of slip between the SAF-CF with a time-lag. These observations indicate that InSAR is a promising tool for monitoring subtle changes of fault coupling and creeping faults are extremely sensitive to small stress perturbations.

Acknowledgments

This research is supported by NASA Earth and Space Science and Technology (FINESST) award 80NSSC19K1330 and USGS NEHRP award G20AP00020.

Open Research/Availability Statement

Sentinel-1 InSAR data used in this study are freely available from European Space Agency (https://scihub.copernicus.eu/dhus/#/home). PBO GPS timeseries solutions are downloaded from UNAVCO (https://www.unavco.org/data/gps-gnss/gps-gnss.html) and Nevada Geodetic Laboratory (http://geodesy.unr.edu/index.php). Creepmeter timeseries solutions are downloaded from USGS (https://earthquake.usgs.gov/monitoring/deformation/data/do

wnload.php). The relocated seismic catalog is searched through the Northern California Earthquake Data Center (NCEDC) (https://www.ncedc.org/ncedc/catalog-search.html). The InSAR data is processed using GMTSAR software. DEM data is downloaded from https://topex.ucsd.edu/gmtsar/demgen/. The North America Land Data Assimilation System (NLDAS) monthly precipitation model (10.5067/Z62LT6J96R4F) is provided by NASA. The high-level Sentinel-1 velocity map and timeseries over the Bay Area produced in this study are available at https://doi.org/10.5281/zenodo.6413342. The characteristic repeating earthquake catalog produced in this study can be found at https://doi.org/10.5281/zenodo.6412692.

Disclaimer

This material is based upon work supported by the U.S. Geological Survey under Grant No. G20AP00020. The views and conclusions contained in this document are those of the authors and should not be interpreted as representing the opinions or policies of the U.S. Geological Survey. Mention of trade names or commercial products does not constitute their endorsement by the U.S. Geological Survey.

References

Amos, C. B., Audet, P., Hammond, W. C., Bürgmann, R., Johanson, I. A., & Blewitt, G. (2014). Uplift and seismicity driven by groundwater depletion in central California. *Nature*, *509*(7501), 483–486. https://doi.org/10.1038/nature13275Ansari, H., Zan, F. De, & Parizzi, A. (2021). Study of Systematic Bias in Measuring Surface Deformation With SAR Interferometry. *IEEE Transactions on Geoscience and Remote Sensing*, *59*(2), 1285–1301. https://doi.org/10.1109/tgrs.2020.3003421Argus, D. F., & Gordon, R. G. (2001). Present tectonic motion across the Coast Ranges and San Andreas fault system in central California. *GSA Bulletin*, *113*(12), 1580–1592. https://doi.org/10.1130/0016-7606(2001)113<1580:PTMATC>2.0.CO;2Baldwin, J., & Bloszies, C. (2022). Tectonic Geomorphic and Quaternary Geologic Mapping of the Quien Sabe Fault, Santa Clara and San Benito Counties, California. *USGS Final Technical Report G21AP10015*, *https://earthquake.usgs.gov/cfusion/external_grants/reports/G21AP10015.pdf*. https://earthquake.usgs.gov/cfusion/external_grants/reports/G21AP10015.pdfBehr, J., Bilham, R., Bodin, P., Burfoid, R. O., & Bürgmann, R. (1990). Aseismic slip on the San Andreas Fault south of Loma Prieta. *Geophysical Research Letters*, *17*(9), 1445–1448. https://doi.org/https://doi.org/10.1029/GL017i009p01445Bekaert, D. P. S., Walters, R. J., Wright, T. J., Hooper, A. J., & Parker, D. J. (2015). Statistical comparison of InSAR tropospheric correction techniques. *Remote Sensing of Environment*, *170*, 40–47. https://doi.org/https://doi.org/10.1016/j.rse.2015.08.035Berardino, P., Fornaro, G., Lanari, R., & Sansosti, E. (2002). A new algorithm for surface deformation monitoring based on small baseline differential SAR interferograms. *IEEE Transactions on Geoscience and Remote Sensing*. https://doi.org/10.1109/TGRS.2002.803792Berrada Baby, H., Golé, P., & Lavergnat, J. (1988). A model for the tropospheric excess path length of

radio waves from surface meteorological measurements. *Radio Science*, *23*(6), 1023–1038. https://doi.org/https://doi.org/10.1029/RS023i006p01023Bilham, R., Suszek, N., & Pinkney, S. (2004). California creepmeters. *Seismological Research Letters*, *75*(4), 481–492.Bilham, R., & Williams, P. (1985). Sawtooth segmentation and deformation processes on the southern San Andreas Fault, California. *Geophysical Research Letters*, *12*(9), 557–560. https://doi.org/https://doi.org/10.1029/GL012i009p00557Blewitt, G., Hammond, W. C., & Kreemer, C. (2018). Harnessing the GPS data explosion for interdisciplinary science. *Eos*, *99*(10.1029), 485.Bokelmann, G. H. R., & Kovach, R. L. (2003). Long-term creep-rate changes and their causes. *Geophysical Research Letters*. https://doi.org/10.1029/2003GL017012Burford, R. O., & Harsh, P. W. (1980). Results of alignment array surveys along the San Andreas fault in Central California in relation to contemporary seismicity. *Bull. Seism. Soc. Am.*, *70*, 1233–1261.Bürgmann, R. (2018). The geophysics, geology and mechanics of slow fault slip. *Earth and Planetary Science Letters*. https://doi.org/10.1016/j.epsl.2018.04.062Chaussard, E., Bürgmann, R., Fattahi, H., Nadeau, R. M., Taira, T., Johnson, C. W., & Johanson, I. (2015). Potential for larger earthquakes in the East San Francisco Bay Area due to the direct connection between the Hayward and Calaveras Faults. *Geophysical Research Letters*, *42*(8), 2734–2741. https://doi.org/10.1002/2015GL063575Chaussard, E, Bürgmann, R., Shirzaei, M., Fielding, E. J., & Baker, B. (2014). Predictability of hydraulic head changes and characterization of aquifer-system and fault properties from InSAR-derived ground deformation. *Journal of Geophysical Research: Solid Earth*, *119*(8), 6572–6590. https://doi.org/https://doi.org/10.1002/2014JB011266Chaussard, Estelle, Milillo, P., Bürgmann, R., Perissin, D., Fielding, E. J., & Baker, B. (2017). Remote Sensing of Ground Deformation for Monitoring Groundwater Management Practices: Application to the Santa Clara Valley During the 2012–2015 California Drought. *Journal of Geophysical Research: Solid Earth*, *122*(10), 8566–8582. https://doi.org/https://doi.org/10.1002/2017JB014676Chen, C. W., & Zebker, H. A. (2002). Phase unwrapping for large SAR interferograms: Statistical segmentation and generalized network models. *IEEE Transactions on Geoscience and Remote Sensing*. https://doi.org/10.1109/TGRS.2002.802453d'Alessio, M. A., Johanson, I. A., Bürgmann, R., Schmidt, D. A., & Murray, M. H. (2005). Slicing up the San Francisco Bay Area: Block kinematics and fault slip rates from GPS-derived surface velocities. *Journal of Geophysical Research: Solid Earth*, *110*(B6). https://doi.org/https://doi.org/10.1029/2004JB003496d'Alessio, M. A., Williams, C. F., & Bürgmann, R. (2006). Frictional strength heterogeneity and surface heat flow: Implications for the strength of the creeping San Andreas fault. *Journal of Geophysical Research: Solid Earth*, *111*(B5). https://doi.org/https://doi.org/10.1029/2005JB003780Du, Y., & Aydin, A. (1993). Stress transfer during three sequential moderate earthquakes along the central Calaveras Fault, California. *Journal of Geophysical Research: Solid Earth*, *98*(B6), 9947–9962. https://doi.org/https://doi.org/10.1029/93JB00154Farr, T. G., Rosen, P. A., Caro, E., Crippen, R., Duren, R., Hensley, S., Kobrick, M., Paller, M., Rodriguez, E., Roth, L., Seal, D., Shaffer, S., Shimada, J.,

Umland, J., Werner, M., Oskin, M., Burbank, D., & Alsdorf, D. (2007). The Shuttle Radar Topography Mission. *Reviews of Geophysics*, *45*(2). https://doi.org/https://doi.org/10.1029/2005RG000183Field, E. H., Arrowsmith, R. J., Biasi, G. P., Bird, P., Dawson, T. E., Felzer, K. R., Jackson, D. D., Johnson, K. M., Jordan, T. H., & Madden, C. (2014). Uniform California earthquake rupture forecast, version 3 (UCERF3)—The time-independent model. *Bulletin of the Seismological Society of America*, *104*(3), 1122–1180.Galehouse, J. S., & Lienkaemper, J. J. (2003). Inferences drawn from two decades of alinement array measurements of creep on faults in the San Francisco Bay region. *Bulletin of the Seismological Society of America*, *93*(6), 2415–2433.Goldstein, R. M., & Werner, C. L. (1998). Radar interferogram filtering for geophysical applications. *Geophysical Research Letters*. https://doi.org/10.1029/1998GL900033Gutenberg, B., & Richter, C. F. (1944). Frequency of earthquakes in California. *Bulletin of the Seismological Society of America*, *34*(4), 185–188.Harris, R. A. (2017). Large earthquakes and creeping faults. In *Reviews of Geophysics*. https://doi.org/10.1002/2016RG000539Hersbach, H., Bell, B., Berrisford, P., Hirahara, S., Horányi, A., Muñoz-Sabater, J., Nicolas, J., Peubey, C., Radu, R., Schepers, D., Simmons, A., Soci, C., Abdalla, S., Abellan, X., Balsamo, G., Bechtold, P., Biavati, G., Bidlot, J., Bonavita, M., … Thépaut, J.-N. (2020). The ERA5 global reanalysis. *Quarterly Journal of the Royal Meteorological Society*, *146*(730), 1999–2049. https://doi.org/https://doi.org/10.1002/qj.3803Johanson, I A, & Bürgmann, R. (2005). Creep and quakes on the northern transition zone of the San Andreas fault from GPS and InSAR data. *Geophysical Research Letters*, *32*(14). https://doi.org/https://doi.org/10.1029/2005GL023150Johanson, Ingrid A., Fielding, E. J., Rolandone, F., & Bürgmann, R. (2006). Coseismic and postseismic slip of the 2004 Parkfield earthquake from space-geodetic data. *Bulletin of the Seismological Society of America*. https://doi.org/10.1785/0120050818Johnson, C. W., Fu, Y., & Bürgmann, R. (2017). Stress Models of the Annual Hydrospheric, Atmospheric, Thermal, and Tidal Loading Cycles on California Faults: Perturbation of Background Stress and Changes in Seismicity. *Journal of Geophysical Research: Solid Earth*, *122*(12), 10,605-610,625. https://doi.org/10.1002/2017jb014778Jolivet, R., Candela, T., Lasserre, C., Renard, F., Klinger, Y., & Doin, M. P. (2015). The burst-like behavior of aseismic slip on a rough fault: The creeping section of the Haiyuan fault, China. *Bulletin of the Seismological Society of America*, *105*(1), 480–488. https://doi.org/10.1785/0120140237Jolivet, R., Grandin, R., Lasserre, C., Doin, M.-P., & Peltzer, G. (2011). Systematic InSAR tropospheric phase delay corrections from global meteorological reanalysis data. *Geophysical Research Letters*, *38*(17). https://doi.org/https://doi.org/10.1029/2011GL048757Jolivet, R., Lasserre, C., Doin, M. P., Peltzer, G., Avouac, J. P., Sun, J., & Dailu, R. (2013). Spatio-temporal evolution of aseismic slip along the Haiyuan fault, China: Implications for fault frictional properties. *Earth and Planetary Science Letters*, *377–378*, 23–33. https://doi.org/10.1016/j.epsl.2013.07.020Jolivet, R., Simons, M.,

Agram, P. S., Duputel, Z., & Shen, Z.-K. (2015). Aseismic slip and seismogenic coupling along the central San Andreas Fault. *Geophysical Research Letters*, *42*(2), 297–306. https://doi.org/https://doi.org/10.1002/2014GL062222Khoshmanesh, M., Shirzaei, M., & Nadeau, R. M. (2015). Time-dependent model of aseismic slip on the central San Andreas Fault from InSAR time series and repeating earthquakes. *Journal of Geophysical Research: Solid Earth*. https://doi.org/10.1002/2015JB012039Khoshmanesh, Mostafa, & Shirzaei, M. (2018). Episodic creep events on the San Andreas Fault caused by pore pressure variations. *Nature Geoscience*, *11*(8), 610–614. https://doi.org/10.1038/s41561-018-0160-2Kreemer, C., Blewitt, G., & Klein, E. C. (2014). A geodetic plate motion and Global Strain Rate Model. *Geochemistry, Geophysics, Geosystems*, *15*(10), 3849–3889. https://doi.org/https://doi.org/10.1002/2014GC005407Li, Y., & Bürgmann, R. (2021). Partial Coupling and Earthquake Potential Along the Xianshuihe Fault, China. *Journal of Geophysical Research: Solid Earth*, *126*(7). https://doi.org/10.1029/2020jb021406Lienkaemper, J J, & Prescott, W. H. (1989). Historic surface slip along the San Andreas fault near Parkfield, California. *Journal of Geophysical Research: Solid Earth*, *94*(B12), 17647–17670.Lienkaemper, James J, Galehouse, J. S., & Simpson, R. W. (1997). Creep Response of the Hayward Fault to Stress Changes Caused by the Loma Prieta Earthquake. *Science*, *276*(5321), 2014–2016. https://doi.org/10.1126/science.276.5321.2014Lindsey, E. O., Fialko, Y., Bock, Y., Sandwell, D. T., & Bilham, R. (2014). Localized and distributed creep along the southern San Andreas Fault. *Journal of Geophysical Research: Solid Earth*, *119*(10), 7909–7922. https://doi.org/10.1002/2014jb011275Lisowski, M., & Prescott, W. H. (1981). Short-range distance measurements along the San Andreas fault system in central California, 1975 to 1979. *Bulletin of the Seismological Society of America*, *71*(5), 1607–1624.Liu, Y.-K., Ross, Z. E., Cochran, E. S., & Lapusta, N. (2022). A unified perspective of seismicity and fault coupling along the San Andreas Fault. *Science Advances*, *8*(8), eabk1167. https://doi.org/10.1126/sciadv.abk1167 PMID - 35196076Liu, Z., Liu, P.-W., Massoud, E., Farr, T. G., Lundgren, P., & Famiglietti, J. S. (2019). Monitoring Groundwater Change in California's Central Valley Using Sentinel-1 and GRACE Observations. In *Geosciences* (Vol. 9, Issue 10). https://doi.org/10.3390/geosciences9100436Lockner, D. A., Morrow, C., Moore, D., & Hickman, S. (2011). Low strength of deep San Andreas fault gouge from SAFOD core. *Nature*, *472*(7341), 82–85. https://doi.org/10.1038/nature09927Materna, K., Feng, L., Lindsey, E. O., Hill, E. M., Ahsan, A., Alam, A. K. M. K., Oo, K. M., Than, O., Aung, T., Khaing, S. N., & Bürgmann, R. (2021). GNSS characterization of hydrological loading in South and Southeast Asia. *Geophysical Journal International*, *224*(3), 1742–1752. https://doi.org/10.1093/gji/ggaa500Materna, K., Taira, T., & Bürgmann, R. (2018). Aseismic Transform Fault Slip at the Mendocino Triple Junction From Characteristically Repeating Earthquakes. *Geophysical Research Letters*, *45*(2), 699–707. https://doi.org/https://doi.org/10.1002/2017GL075899McFarland, F.S., Lienkaemper, J.J., Caskey, S.J., and Elliot, A. J. (2017). Data from theodolite

measurements of creep rates on San Francisco Bay region faults, California. In *U.S. Geological Survey data release,*. https://doi.org/10.3133/ofr20091119Mongovin, D. D., & Philibosian, B. (2021). Creep on the Sargent Fault over the Past 50 Yr from Alignment Arrays with Implications for Slip Transfer between the Calaveras and San Andreas Faults, California. *Bulletin of the Seismological Society of America*, *111*(6), 3189–3203. https://doi.org/10.1785/0120210041Moore, D. E., & Rymer, M. J. (2007). Talc-bearing serpentinite and the creeping section of the San Andreas fault. *Nature*. https://doi.org/10.1038/nature06064Murray-Moraleda, J. R., & Simpson, R. W. (2009). Geodetically Inferred Coseismic and Postseismic Slip due to the M 5.4 31 October 2007 Alum Rock Earthquake. *Bulletin of the Seismological Society of America*, *99*(5), 2784–2800. https://doi.org/10.1785/0120090017Nadeau, R. M., & Johnson, L. R. (1998). Seismological studies at Parkfield VI: Moment release rates and estimates of source parameters for small repeating earthquakes. *Bulletin of the Seismological Society of America*, *88*(3), 790–814. https://doi.org/10.1785/BSSA0880030790Nadeau, R. M., & McEvilly, T. V. (2004). Periodic Pulsing of Characteristic Microearthquakes on the San Andreas Fault. *Science*, *303*(5655), 220–222. https://doi.org/10.1126/science.1090353 PMID - 14716011Ojha, C., Shirzaei, M., Werth, S., Argus, D. F., & Farr, T. G. (2018). Sustained Groundwater Loss in California's Central Valley Exacerbated by Intense Drought Periods. *Water Resources Research*, *54*(7), 4449–4460. https://doi.org/https://doi.org/10.1029/2017WR022250Oppenheimer, D. H., Bakun, W. H., & Lindh, A. G. (1990). Slip partitioning of the Calaveras Fault, California, and prospects for future earthquakes. *Journal of Geophysical Research: Solid Earth*, *95*(B6), 8483–8498. https://doi.org/https://doi.org/10.1029/JB095iB06p08483Prescott, W., & Burford, R. (1976). Slip on the Sargent Fault. *Bulletin of the Seismological Society of America*, *44*(1), 123–134. https://doi.org/https://doi.org/10.1785/BSSA0660031013 PMID - 7823326Provost, A.-S., & Houston, H. (2001). Orientation of the stress field surrounding the creeping section of the San Andreas Fault: Evidence for a narrow mechanically weak fault zone. *Journal of Geophysical Research: Solid Earth*, *106*(B6), 11373–11386. https://doi.org/https://doi.org/10.1029/2001JB900007Roeloffs, E. A. (2001). Creep rate changes at Parkfield, California 1966–1999: Seasonal, precipitation induced, and tectonic. *Journal of Geophysical Research: Solid Earth*, *106*(B8), 16525–16547. https://doi.org/https://doi.org/10.1029/2001JB000352Roland, B., D., S., M., N. R., M., d'Alessio, E., F., D., M., V., M. T., & H., M. M. (2000). Earthquake Potential Along the Northern Hayward Fault, California. *Science*, *289*(5482), 1178–1182. https://doi.org/10.1126/science.289.5482.1178Ryder, I., & Bürgmann, R. (2008). Spatial variations in slip deficit on the central San Andreas Fault from InSAR. *Geophysical Journal International*, *175*(3), 837–852. https://doi.org/10.1111/j.1365-246X.2008.03938.xSandwell, D., Mellors, R., Tong, X., Wei, M., & Wessel, P. (2011a). *GMTSAR: An InSAR Processing System Based on Generic Mapping Tools*. Eos Trans. AGU.Sandwell, D., Mellors, R., Tong, X., Wei, M., & Wessel, P. (2011b). Open radar interferometry software for mapping surface Deformation. *Eos, Transactions American Geophysical Union*. https://doi.org/10.1029/2011eo280002Savage, J. C., & Burford, R. O. (1973). Geodetic determination of relative plate motion in

central California. *Journal of Geophysical Research (1896-1977)*, *78*(5), 832–845. https://doi.org/https://doi.org/10.1029/JB078i005p00832Savage, J. C., & Lisowski, M. (1993). Inferred depth of creep on the Hayward Fault, central California. *Journal of Geophysical Research*. https://doi.org/10.1029/92JB01871Schmidt, D. A., & Bürgmann, R. (2003). Time-dependent land uplift and subsidence in the Santa Clara valley, California, from a large interferometric synthetic aperture radar data set. *Journal of Geophysical Research: Solid Earth*. https://doi.org/10.1029/2002jb002267Schorlemmer, D., Wiemer, S., & Wyss, M. (2004). Earthquake statistics at Parkfield: 1. Stationarity of b values. *Journal of Geophysical Research: Solid Earth*, *109*(B12). https://doi.org/https://doi.org/10.1029/2004JB003234Schulz, S. S. (1989). Catalog of creepmeter measurements in California from 1966 through 1988. In *Open-File Report*. https://doi.org/10.3133/ofr89650Scott, C. P., DeLong, S. B., & Arrowsmith, J. R. (2020). Distribution of Aseismic Deformation Along the Central San Andreas and Calaveras Faults From Differencing Repeat Airborne Lidar. *Geophysical Research Letters*, *47*(22). https://doi.org/10.1029/2020gl090628Shah, A. K., & Boyd, O. S. (2018). Depth to basement and thickness of unconsolidated sediments for the western United States—Initial estimates for layers of the U.S. Geological Survey National Crustal Model. In *Open-File Report*. https://doi.org/10.3133/ofr20181115Shirzaei, M., & Bürgmann, R. (2013). Time-dependent model of creep on the Hayward fault from joint inversion of 18 years of InSAR and surface creep data. *Journal of Geophysical Research: Solid Earth*, *118*(4), 1733–1746. https://doi.org/10.1002/jgrb.50149Shirzaei, Manoochehr, Bürgmann, R., & Taira, T. (2013). Implications of recent asperity failures and aseismic creep for time-dependent earthquake hazard on the Hayward fault. *Earth and Planetary Science Letters*, *371*, 59–66.Simpson, R. W., Lienkaemper, J. J., & Galehouse, J. S. (2001). Variations in creep rate along the Hayward Fault, California, interpreted as changes in depth of creep. *Geophysical Research Letters*, *28*(11), 2269–2272. https://doi.org/https://doi.org/10.1029/2001GL012979Taira, T., Bürgmann, R., Nadeau, R. M., & Dreger, D. S. (2014). Variability of fault slip behavior along the San Andreas Fault in the San Juan Bautista Region. *Journal of Geophysical Research: Solid Earth*. https://doi.org/10.1002/2014JB011427Templeton, D. C., Nadeau, R. M., & Bürgmann, R. (2008a). Behavior of repeating earthquake sequences in Central California and the implications for subsurface fault creep. *Bulletin of the Seismological Society of America*, *98*(1), 52–65. https://doi.org/10.1785/0120070026Templeton, D. C., Nadeau, R. M., & Bürgmann, R. (2008b). Behavior of Repeating Earthquake Sequences in Central California and the Implications for Subsurface Fault Creep. *Bulletin of the Seismological Society of America*, *98*(1), 52–65. https://doi.org/10.1785/0120070026Thatcher, W., Marshall, G., & Lisowski, M. (1997). Resolution of fault slip along the 470-km-long rupture of the great 1906 San Francisco earthquake and its implications. *Journal of Geophysical Research B: Solid Earth*, *102*(B3), 5353–5367.

http://pubs.er.usgs.gov/publication/70019238Thomas, A. M., Bürgmann, R., Shelly, D. R., Beeler, N. M., & Rudolph, M. L. (2012). Tidal triggering of low frequency earthquakes near Parkfield, California: Implications for fault mechanics within the brittle-ductile transition. *Journal of Geophysical Research: Solid Earth*, *117*(B5). https://doi.org/https://doi.org/10.1029/2011JB009036Titus, S. J., DeMets, C., & Tikoff, B. (2006). Thirty-five-year creep rates for the creeping segment of the San Andreas fault and the effects of the 2004 Parkfield earthquake: Constraints from alignment arrays, continuous global positioning system, and creepmeters. *Bulletin of the Seismological Society of America*, *96*(4B), S250–S268.Tong, X., Sandwell, D. T., & Smith-Konter, B. (2013). High-resolution interseismic velocity data along the San Andreas Fault from GPS and InSAR. *Journal of Geophysical Research: Solid Earth*. https://doi.org/10.1029/2012JB009442Toppozada, T. R., Branum, D. M., Reichle, M. S., & Hallstrom, C. L. (2002). San Andreas Fault Zone, California: M 5.5 Earthquake History. *Bulletin of the Seismological Society of America*, *92*(7), 2555–2601. https://doi.org/10.1785/0120000614Tormann, T., Wiemer, S., & Mignan, A. (2014). Systematic survey of high-resolution b value imaging along Californian faults: Inference on asperities. *Journal of Geophysical Research: Solid Earth*, *119*(3), 2029–2054. https://doi.org/https://doi.org/10.1002/2013JB010867Turner, R C, Nadeau, R. M., & Bürgmann, R. (2013). Aseismic slip and fault interaction from repeating earthquakes in the Loma Prieta aftershock zone. *Geophysical Research Letters*, *40*(6), 1079–1083. https://doi.org/10.1002/grl.50212Turner, Ryan C, Shirzaei, M., Nadeau, R. M., & Bürgmann, R. (2015). Slow and Go: Pulsing slip rates on the creeping section of the San Andreas Fault. *Journal of Geophysical Research: Solid Earth*, *120*(8), 5940–5951. https://doi.org/https://doi.org/10.1002/2015JB011998Tymofyeyeva, E., & Fialko, Y. (2015). Mitigation of atmospheric phase delays in InSAR data, with application to the eastern California shear zone. *Journal of Geophysical Research: Solid Earth*, *120*(8), 5952–5963. https://doi.org/10.1002/2015JB011886Tymofyeyeva, E., Fialko, Y., Jiang, J., Xu, X., Sandwell, D., Bilham, R., Rockwell, T. K., Blanton, C., Burkett, F., Gontz, A., & Moafipoor, S. (2019). Slow Slip Event On the Southern San Andreas Fault Triggered by the 2017 Mw8.2 Chiapas (Mexico) Earthquake. *Journal of Geophysical Research: Solid Earth*, *124*(9), 9956–9975. https://doi.org/10.1029/2018JB016765Uchida, N. (2019). Detection of repeating earthquakes and their application in characterizing slow fault slip. *Progress in Earth and Planetary Science*, *6*(1), 40. https://doi.org/10.1186/s40645-019-0284-zUchida, N., & Bürgmann, R. (2019). Repeating Earthquakes. *Annual Review of Earth and Planetary Sciences*, *47*(1), 305–332. https://doi.org/10.1146/annurev-earth-053018-060119Waldhauser, F. (2009). Near-Real-Time Double-Difference Event Location Using Long-Term Seismic Archives, with Application to Northern California. *Bulletin of the Seismological Society of America*, *99*(5), 2736–2748. https://doi.org/10.1785/0120080294Waldhauser, F., & Schaff, D. P. (2008). Large-scale relocation of two decades of Northern California seismicity using cross-correlation and double-difference

methods. *Journal of Geophysical Research: Solid Earth*, *113*(B8). https://doi.org/https://doi.org/10.1029/2007JB005479Waldhauser, F., & Schaff, D. P. (2021). A Comprehensive Search for Repeating Earthquakes in Northern California: Implications for Fault Creep, Slip Rates, Slip Partitioning, and Transient Stress. *Journal of Geophysical Research: Solid Earth*, *126*(11). https://doi.org/10.1029/2021jb022495Wallace, R. E. (1990). *The San Andreas fault system, California*. Department of the Interior, US Geological Survey.Watt, J. T., Ponce, D. A., Graymer, R. W., Jachens, R. C., & Simpson, R. W. (2014). Subsurface geometry of the San Andreas-Calaveras fault junction: Influence of serpentinite and the Coast Range Ophiolite. *Tectonics*, *33*(10), 2025–2044. https://doi.org/https://doi.org/10.1002/2014TC003561Wei, M., Sandwell, D., & Fialko, Y. (2009). A silent Mw 4.7 slip event of October 2006 on the Superstition Hills fault, southern California. *Journal of Geophysical Research: Solid Earth*. https://doi.org/10.1029/2008JB006135Wiemer, S., & Wyss, M. (2000). Minimum Magnitude of Completeness in Earthquake Catalogs: Examples from Alaska, the Western United States, and Japan. *Bulletin of the Seismological Society of America*, *90*(4), 859–869. https://doi.org/10.1785/0119990114Xia, Y., Mitchell, K., Ek, M., Sheffield, J., Cosgrove, B., Wood, E., Luo, L., Alonge, C., Wei, H., & Meng, J. (2012). Continental-scale water and energy flux analysis and validation for the North American Land Data Assimilation System project phase 2 (NLDAS-2): 1. Intercomparison and application of model products. *Journal of Geophysical Research: Atmospheres*, *117*(D3).Zaliapin, I., & Ben-Zion, Y. (2013). Earthquake clusters in southern California I: Identification and stability. *Journal of Geophysical Research: Solid Earth*, *118*(6), 2847–2864. https://doi.org/10.1002/jgrb.50179Zhang, E., Fuis, G. S., Catchings, R. D., Scheirer, D. S., Goldman, M., & Bauer, K. (2018). Reexamination of the subsurface fault structure in the vicinity of the 1989 moment-magnitude-6.9 Loma Prieta earthquake, central California, using steep-reflection, earthquake, and magnetic data. In *Open-File Report*. https://doi.org/10.3133/ofr20181093